ESAIM: M2AN 53 (2019) 1797–1840
https://doi.org/10.1051/m2an/2019040

ESAIM: Mathematical Modelling and Numerical Analysis
www.esaim-m2an.org

DISCRETE DUALITY FINITE VOLUME METHOD WITH TANGENTIAL REDISTRIBUTION OF POINTS FOR SURFACES EVOLVING BY MEAN CURVATURE

Lukáš Tomek[1,*] and Karol Mikula[1]

Abstract. We propose a new discrete duality finite volume method for solving mean curvature flow of surfaces in $\mathbb{R}^3$. In the cotangent scheme, which is widely used discretization of Laplace–Beltrami operator, a two-dimensional surface is usually approximated by a triangular mesh. In the cotangent scheme the unknowns are the vertices of the triangulation. A finite volume around each vertex is constructed as a surface patch bounded by a piecewise linear curve with nodes in the midpoints of the neighbouring edges and a representative point of each adjacent triangle. The basic idea of our new approach is to include the representative points into the numerical scheme as supplementary unknowns and generalize discrete duality finite volume method from $\mathbb{R}^2$ to 2D surfaces embedded in $\mathbb{R}^3$. To improve the quality of the mesh we use an area-oriented tangential redistribution of the grid points. We derive the numerical scheme for both closed surfaces and surfaces with boundary, and present numerical experiments. Surface evolution models are applied to construction of minimal surfaces with given set of boundary curves.

Mathematics Subject Classification. 53A10, 53C44, 65D17, 65M08.

Received October 11, 2018. Accepted June 6, 2019.

1. Introduction

The main goal of the paper is to derive a Discrete duality finite volume (DDFV) method for numerical solution of the mean curvature flow of surfaces in $\mathbb{R}^3$

$$\partial_t \varphi = \triangle_{g_\varphi} \varphi, \tag{1.1}$$

where φ is a position vector of a point on the surface, $\partial_t \varphi$ is the velocity of the point, $h = \triangle_{g_\varphi} \varphi$ is the mean curvature vector in the point φ and $\triangle_{g_\varphi}$ denotes the Laplace–Beltrami operator. We enrich the mean curvature flow with suitable tangential velocity in order to redistribute the mesh points along the surface, which is crucial for stability of numerical computations. The redistribution technique proposed for our DDFV method is based on the area-oriented tangential redistribution. For the cotangent scheme it was developed in the paper [27] for closed surfaces and it was also used for surfaces with boundary by Tomek *et al.* [43].

Keywords and phrases. Surface evolution, mean curvature flow, tangential redistribution, finite volume, discrete duality, minimal surface.

[1] Faculty of Civil Engineering, Slovak University of Technology, Radlinského 11, 811 07 Bratislava, Slovak Republic.
*Corresponding author: tomek@math.sk

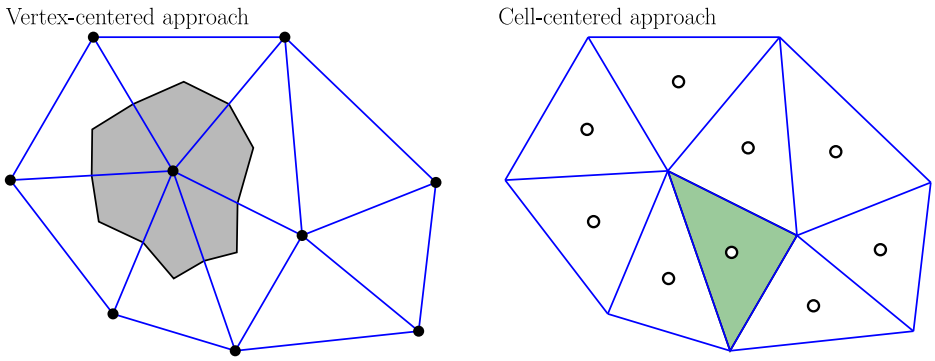

FIGURE 1. *Left panel*: vertex-centered approach, unknowns at vertices of the primal mesh (*blue*) and a dual cell (finite volume) associated to a vertex (*grey*). *Right panel*: cell-centered approach, unknowns at centers of the primal mesh and a primal cell (*green*) (Color online).

The mean curvature flow (1.1) may be regarded as a sort of geometric heat equation. On the other hand, the mean curvature flow is not really equivalent to a heat equation, since the Laplace–Beltrami operator evolves with the surface itself.

The mean curvature flow was originally proposed as a model for description of the evolution of the interfaces in multiphase physical models (see [33]). Since minimal surfaces (surfaces with zero mean curvature) are the critical points for the mean curvature flow, one can use the mean curvature flow as a tool for constructing minimal surfaces with given boundary curve. Such surfaces are used, *e.g.*, in architecture (see [21,36,47]). The problem of finding a minimal surface with given set of boundary curves is called the Plateau problem, named after the Belgian physicist J.A.F. Plateau who made experimental studies of soap films (see [38]). Convergence of discrete approximations of minimal surfaces was explored in [13,39,44]. Algorithms based on the mean curvature flow have also been developed in the field of digital image processing because of the "regularizing effect" due to its parabolic nature (see [1,7,26]).

Two basic approaches are used for solving manifold evolution problems (including mean curvature flow of surfaces in $\mathbb{R}^3$), the Lagrangian approach that evolves the manifold directly (see [2,12,15,27]) and the Eulerian (level set) approach that, in general, considers the n-dimensional manifold as a level set of a function of $n+1$ variables (see [7,16,26,35,40]). This work follows the Lagrangian approach.

The numerical methods for solving the equation (1.1) are usually based on a finite element method (see [2,12,14]) or a finite volume method (see [21,25,27]). In this work we deal with finite volume methods. Given a (primal) mesh, finite volume methods for the equation (1.1) may be classified into two main distinct categories: "vertex-centered" methods and "cell-centered" methods. Vertex-centered methods compute approximate values of φ at the vertices of the primal mesh by integrating the time-discretized version of equation (1.1) on dual cells (finite volumes) associated to the vertices of the primal mesh (Fig. 1, *left*). On the opposite, cell-centered methods compute approximate values of φ at the centers of the cells of the primal mesh by integrating the equation on the primal cells (Fig. 1, *right*). For a review of these methods, we refer to [17]. Regarding the placement of cell centers, many choices are available. One can use the barycenter or circumceter of the triangle, or apply quite recent approach called Hodge-optimized triangulations [32].

In the paper [9] the authors study a specific cell-centered method, the so-called diamond-cell method. A diamond cell is a quadrilateral cell associated with an edge of the primal mesh and is obtained by joining the two vertices of this edge with the centers of the two cells of the primal mesh which share this edge (Fig. 2). In finite volume methods, the integral of $\triangle\varphi$ over the primal cell is rewritten using the divergence theorem to the integral of $\nabla\varphi \cdot \nu$ over the boundary of the cell, ν denoting the outward normal to the boundary of the cell. Therefore one needs an approximation of $\nabla\varphi$ on the edges of the primal mesh. The gradient $\nabla\varphi$ is approximated by the

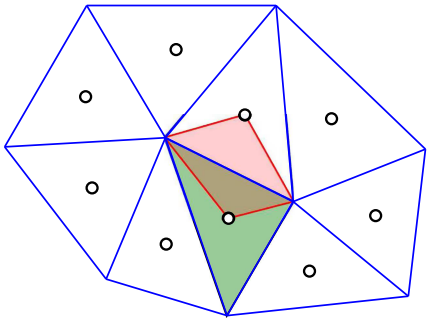

FIGURE 2. A diamond cell (*red*) associated to an edge of the primal mesh (*blue*) (Color online).

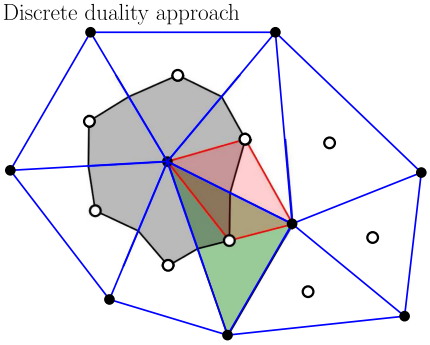

FIGURE 3. Discrete duality method, unknowns both in vertices and and cell centers of the primal mesh (Color online).

mean value of the gradient over a diamond cell, which is defined with the help of the values of the function φ at the centers and at the vertices of the primal cells. The discrete solution at the vertices of the primal mesh is computed by an interpolation of its values at the centers of the neighbouring cells. The advantage of this scheme is that it can be used on almost arbitrary two-dimensional grids and extends naturally to three dimensions.

In the papers [10, 11, 18] the authors develop a discrete duality finite volume (DDFV) method which is a fusion of the vertex-centered and cell-centered approach. They start by adopting the diamond-mesh technique to reconstruct the gradient $\nabla\varphi$, but instead of interpolating the values of φ at the vertices of the primal mesh, they consider these values as supplementary unknowns of the numerical scheme (Fig. 3). Therefore, they also have to write an equivalent number of supplementary equations. These are obtained by integrating the equation, not only on the cells of the primal mesh, but also on the cells of the dual mesh. In both integrations the same approximation of the gradient $\nabla\varphi$ is used. Since the approximation of the gradient on a diamond cell uses the values of φ in vertices as well as cell centers of the primal mesh, the final system of equations is coupled.

Note that even if the DDFV approach starts by fixing a primary mesh and constructing successively the dual and diamond meshes, the diamond mesh can be interpreted as a central object since its choice fixes both primal and dual meshes.

In this paper we present a DDFV method for surfaces embedded in $\mathbb{R}^3$. Contrarily to the standard setting of heat-like parabolic equations, in our problem (1.1) the mesh evolves with the solution itself. It is therefore reasonable to monitor the location of the cell centers at each time step. Our idea is to let the PDE itself evolve the mesh centers rather than to make simple ad hoc choices like sticking to barycenter at each time step. Another important motivation for a new finite volume method for the mean curvature flow rises from

the fact that the finite volumes in the widely used vertex-centered method, the so-called cotangent scheme (see [25]), are not defined uniquely, which leads to non-uniqueness of the definition of the mean curvature. This can cause a serious problem, because the mean curvature is often used in further calculations (*e.g.* in tangential redistribution techniques). The non-uniqueness is following: the "cell center" of a triangle (cell of the primal mesh) used for the construction of the finite volume (cell of the dual mesh) can lie anywhere in the triangle and the integral of the term $\triangle_{g_\varphi}\varphi$ in (1.1) over the finite volume is the same. Since, in the discrete differential geometry, the mean curvature vector is then approximated by dividing the integral by the area of the finite volume (which is not defined uniquely), it leads to a nonunique value of the mean curvature depending on the choice of the "cell center". In our scheme we remove this non-uniqueness by including the cell centers to unknowns of the numerical scheme.

To improve the quality of the discretization mesh, which is crucial for stability and precision of computation in Lagrangian approach, various techniques for tangential redistribution of points have been developed for curves evolving in two dimensions (see [3, 5, 20, 23, 29, 41, 46]), three dimensions (see [19, 28]) or on 2D surfaces (see [6, 30, 34]). A lot of work has been done for surfaces evolving in $\mathbb{R}^3$ (see [2, 22, 31]).

The DDFV method for mean curvature flow of surfaces with no tangential redistribution was outlined in a conference proceedings paper, see [42]. In this paper we provide a derivation of the scheme with all details and develop a suitable tangential redistribution for DDFV method.

The text of this paper is organized in four main sections. In Section 2 we introduce the mathematical model. Some parts of this section can be found in the papers [27, 42, 43] but to make the text self-content we summarize the ideas also here. In the Section 3 we review well known cotangent scheme and give a motivation for a new scheme. In the Section 4 we present a Discrete duality finite volume method with an area-oriented tangential redistribution. Complete derivation of the numerical scheme is in Section 4.1 and discretization of the tangential velocity is in Section 4.2. The Section 5 gives numerical experiments illustrating the basic properties of the method and the effect of the tangential redistribution. Both experiments with closed surfaces as well as surfaces with boundary are included. The method is applied to construction of several minimal surfaces with given set of boundary curves. Some experiments from [42] are present also in this paper with the purpose of comparison to the experiments with tangential redistribution.

2. Mathematical model

2.1. Manifold evolution

Let $\varphi^0 : X \to Y$ be a smooth immersion of a m-dimensional Riemannian manifold (X, g_X) into n-dimensional Riemannian manifold (Y, g_Y), $m \leq n$. The evolution of $X^0 = \varphi^0(X)$ is a one-parameter family of immersions $\varphi : X \times [0, t_f] \to Y$. Given a fixed point $x \in X$, the map $x \mapsto \varphi(x) = \varphi(x, .)$, is a smooth curve on Y. Let $v^t(x)$ denote the vector tangential to the curve at the point $\varphi^t(x) = \varphi(x, t)$ (see Fig. 4), where the map $\varphi^t : X \to Y$ represents a selected immersion from the whole family of immersions. The map $v : X \times [0, t_f] \to TY$, where TY is the tangent bundle of Y, represents the velocity field of the evolution. Thus, the map φ is a solution of the equation

$$\partial_t \varphi = v. \tag{2.1}$$

The evolution equation (2.1) is coupled with an initial condition $\varphi(x, 0) = \varphi^0(x)$ and, for a manifold X with boundary, with a Dirichlet boundary condition

$$\varphi(x, t) = \varphi^0(x), \qquad x \in \partial X, t \in [0, t_f], \tag{2.2}$$

meaning the boundary is static. It is convenient to rewrite the velocity v in the form

$$\partial_t \varphi = v_N + v_T, \tag{2.3}$$

where v_N and v_T are the velocities of the evolution in the normal and tangential direction to the immersed manifold $X^t = \varphi^t(X)$ respectively (Fig. 4). Whereas the normal velocity v_N has an effect on the position and

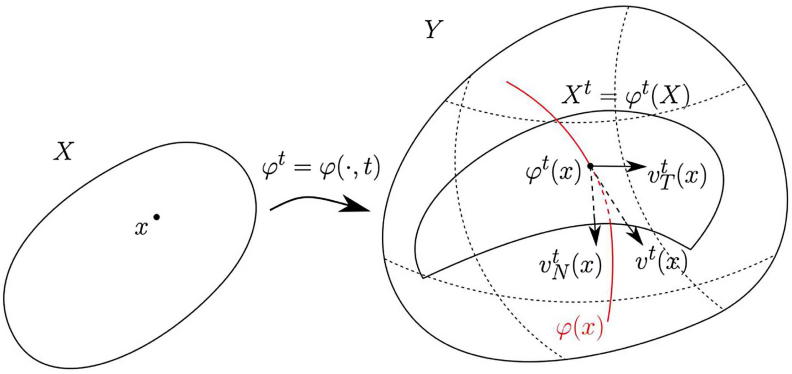

FIGURE 4. Evolution of a manifold X in a manifold Y.

the shape of the immersed manifold X^t, the tangential velocity v_T only moves the points along X^t. In the discrete setting, the tangential velocity v_T can be designed to control the distribution of the mesh vertices, which becomes crucial in numerical computations. An inappropriate placement of the mesh vertices can lead to unacceptable errors or even to a crash of the computation process.

2.2. Mean curvature flow

The special type of the evolution model (2.3) is the mean curvature flow of surfaces in $\mathbb{R}^3$. That means, X is a two-dimensional manifold (possibly with boundary) and $Y = \mathbb{R}^3$ with standard Euclidean metric tensor g_Y (*i.e.* $g_Y(u, v) = u \cdot v$, with dot denoting the standard inner product of vectors $u, v \in \mathbb{R}^3$). The unknown $\varphi(x, t)$ is a position vector in $\mathbb{R}^3$ which satisfies the evolution model

$$\begin{aligned} \partial_t \varphi &= h, \\ \text{with} \quad \varphi(x, 0) &= \varphi^0(x), \qquad x \in X, \end{aligned} \tag{2.4}$$

which means the flow is driven by the normal velocity field $v_N = h$, where the quantity $h(x, t) = H(x, t)N(x, t)$ is called mean curvature vector, with $H(x, t)$ and $N(x, t)$ being respectively the mean curvature and the unit normal[2] of the surface $X^t = \varphi^t(X)$ at the point $x \in X$, see Figure 5. The mean curvature at a given point is the sum of the principal curvatures

$$H = \kappa_{\max} + \kappa_{\min}. \tag{2.5}$$

In case of the closed surface, the model (2.4) leads to a shrinking of the volume enclosed by the surface. For a surface with boundary, the model (2.4) is coupled with a Dirichlet boundary condition (2.2). The mean curvature vector can be computed from the embedding φ using the formula (see *e.g.* [24])

$$h = \triangle_{g_\varphi} \varphi, \tag{2.6}$$

where $\triangle_{g_\varphi}$ denotes the Laplace–Beltrami operator associated with the metric tensor $g_{\varphi^t} = (\varphi^t)^* g_Y$ induced by the immersion φ^t, where $(\varphi^t)^*$ denotes the pullback by φ^t. To simplify the notation we usually omit the time index t if g_{φ^t} is a subscript (as in Laplace–Beltrami operator in (2.6)). Using (2.6) we can rewrite the

[2]The orientation of the normal does not matter in this paper, because we will use the formula (2.6) to calculate the mean curvature vector and the mean curvature will be calculated as $H = h \cdot N$. However, one has to be careful when reading literature. Depending on the author's convention, the model (2.4) reads $\partial_t \varphi = HN$ or $\partial_t \varphi = -HN$. If the outward normal is considered, the model $\partial_t \varphi = -HN$ is correct, so that the sphere (being a surface with constant positive mean curvature) shrinks under the mean curvature flow.

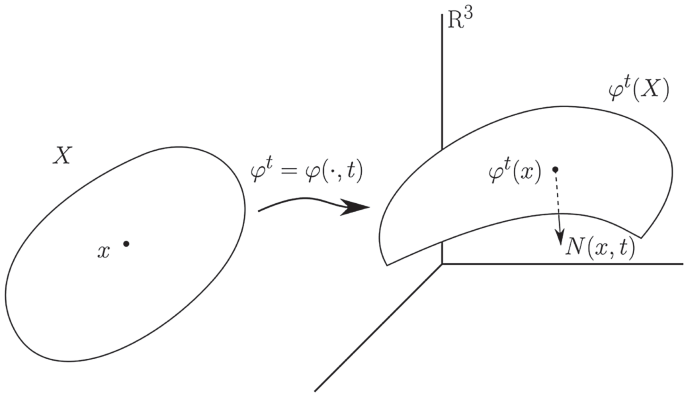

FIGURE 5. Evolution of a 2-dimensional manifold X in $\mathbb{R}^3$.

model (2.4) to the form

$$\begin{aligned} \partial_t \varphi &= \triangle_{g_\varphi} \varphi, \\ \text{with} \quad \varphi(x,0) &= \varphi^0(x), \qquad x \in X. \end{aligned} \tag{2.7}$$

2.3. The area-oriented tangential redistribution

In our problem only the normal velocity of the evolution is given, $v = HN$. Thus we can enrich the model (2.7) with a suitable tangential velocity v_T

$$\partial_t \varphi = \triangle_{g_\varphi} \varphi + v_T \tag{2.8}$$

in order to control the mesh quality of the discretized evolving manifold.

On the manifold X we have the metric g_X and the measure ξ induced by g_X. The metric tensor g_{φ^t} induces another measure χ_{φ^t} on X. These two measures are related by the following formula

$$\mathrm{d}\chi_{\varphi^t} = G^t \mathrm{d}\xi, \tag{2.9}$$

where the map G^t is called volume density of the immersion φ^t in general, and in case of evolving surfaces we will call it area density. The area of a measurable set $U \subseteq X$ is calculated as

$$\chi_{\varphi^t}(U) = \int_U \mathrm{d}\chi_{\varphi^t} = \int_U G^t \mathrm{d}\xi. \tag{2.10}$$

Specially, the global area of X measured by the measure χ_{φ^t} is

$$A^t = \int_X \mathrm{d}\chi_{\varphi^t} = \int_X G^t \mathrm{d}\xi. \tag{2.11}$$

In the paper [27] the authors design an area-oriented tangential redistribution to control the relative area

$$\frac{\chi_{\varphi^t}(U)}{A^t} \tag{2.12}$$

of *any* subset $U \subseteq X$ throughout the evolution. Since the subset U is arbitrary, controlling the relative areas implies controlling the ratio

$$\frac{G^t(x)}{A^t}, \qquad \text{for almost all } x \in X. \tag{2.13}$$

In order to investigate (and control) the evolution of the ratio (2.13) we need to calculate the time derivative of the area density G^t and the total area A^t. According to Bauer *et al.* [4], the area density G^t satisfies the following equation

$$\partial_t G = (-g_Y(v_N, h) + \mathrm{div}_{g_\varphi} w_T)G, \tag{2.14}$$

where w_T is the tangential vector field on X and the operator div_{g_φ} represents the divergence on X associated to the induced metric g_φ. The tangential vector field v_T on $X^t \subset Y$ is obtained as $v_T = \varphi^t_* w_T$, *i.e.* the pushforward of w_T along the map φ^t. From (2.14) we get the evolution equation for the global area

$$\partial_t A = -\int_X g_Y(v_N, h)\mathrm{d}\chi_\varphi + \int_{\partial X} g_\varphi(w_T, \nu)\mathrm{d}H_\chi, \tag{2.15}$$

where $H_{\chi_{\varphi^t}}$ is the $(m-1)$-dimensional Hausdorff measure on ∂X induced by χ_{φ^t} and ν is the outward unit normal (with respect to g_φ) to the boundary ∂X. In case of a closed surface ($\partial X = \emptyset$) the second integral vanishes. In case of a manifold with static boundary, the component of the tangential velocity w_T normal to the boundary vanishes

$$g_\varphi(w_T, \nu)|_{\partial X} = 0, \tag{2.16}$$

so for both cases the formula (2.15) reduces to

$$\partial_t A = -\int_X g_Y(v_N, h)\mathrm{d}\chi_\varphi. \tag{2.17}$$

If we want to conserve the relative areas, we can require (see [27, 46])

$$\partial_t \left(\frac{G}{A}\right) = 0. \tag{2.18}$$

Using the formulas (2.14) and (2.17) in (2.18) we obtain the equation for divergence of the tangential velocity

$$\mathrm{div}_{g_\varphi} w_T = g_Y(v_N, h) - \langle g_Y(v_N, h)\rangle_{\chi_\varphi}, \tag{2.19}$$

where $\langle\,.\,\rangle_{\chi_\varphi}$ denotes the mean over X with respect to the measure χ_φ, *i.e.*

$$\langle g_Y(v_N, h)\rangle_{\chi_\varphi} = \frac{1}{A}\int_X g_Y(v_N, h)\mathrm{d}\chi_\varphi. \tag{2.20}$$

From a discrete point of view, the relative area conserving redistribution (2.19) might be convenient if we are satisfied with the initial quality of the discretization of X (in sense of relative areas) and want to preserve the relative areas of the polygons.

In many situations it is practical to have some sort of uniform discretization. For example, uniform mesh is appropriate for surfaces with constant mean curvature, *e.g.* minimal surfaces (having zero mean curvature) which will be constructed in this paper. In terms of area density, a uniform discretization satisfies

$$\frac{G^t(x)}{A^t} \underset{t\to\infty}{\longrightarrow} C, \qquad \text{for almost all } x \in X, \tag{2.21}$$

where $C \in \mathbb{R}_+$, *i.e.* the relative areas become constant over X as the time tends to infinity. The value of the constant C can be computed easily. The equation (2.11) implies $\int_X \frac{G^t}{A^t}\mathrm{d}\xi = 1$, taking the limit $t \to \infty$ gives $C\int_X \mathrm{d}\xi = 1$ and therefore $C = \frac{1}{\xi(X)}$, where $\xi(X) = \int_X \mathrm{d}\xi$ is the total area of X computed with respect to the measure ξ. The limit (2.21) holds, *e.g.*, if the ratio G/A is a solution of the following equation (see [27, 29])

$$\partial_t \left(\frac{G}{A}\right) = \left(C - \frac{G}{A}\right)\omega, \tag{2.22}$$

where ω is a nonnegative constant controlling the speed of the redistribution. Combining (2.22) with (2.14) and (2.17) one gets the formula for divergence of w_T

$$\mathrm{div}_{g_\varphi} w_T = g_Y(v_N, h) - \langle g_Y(v_N, h)\rangle_{\chi_\varphi} + \left(C\frac{A}{G} - 1\right)\omega. \tag{2.23}$$

Note that since the condition (2.18) is a special case of (2.22) for $\omega = 0$, the formula (2.19) for relative area preserving redistribution can be achieved from (2.23) as a special case.

The conditions (2.19) and (2.23) do not determine w_T uniquely. We assume that velocity field w_T is a gradient field

$$w_T^t = \nabla_{g_{\varphi^t}} \psi^t, \tag{2.24}$$

where $\psi^t : X \to \mathbb{R}$ is a potential of the vector field w_T^t. Under this assumption, we get the following equation for velocity potential ψ^t

$$\triangle_{g_\varphi} \psi = g_Y(v_N, h) - \langle g_Y(v_N, h)\rangle_{\chi_\varphi} \tag{2.25}$$

for the relative area preserving redistribution and

$$\triangle_{g_\varphi} \psi = g_Y(v_N, h) - \langle g_Y(v_N, h)\rangle_{\chi_\varphi} + \left(C\frac{A}{G} - 1\right)\omega \tag{2.26}$$

for the asymptotically uniform redistribution. In order to guarantee the uniqueness of ψ^t, the equation (2.25) or (2.26) is accompanied with an appropriate condition. We may prescribe the value of ψ^t in one selected point

$$\psi^t(p) = 0, \qquad p \in X. \tag{2.27}$$

We could use $\psi^t(p) = c$ with any $c \in \mathbb{R}$, because the gradient $w_T^t = \nabla_{g_{\varphi^t}} \psi^t$ is independent of this choice. The other possibility is to fix the mean value of ψ^t over X

$$\langle \psi^t \rangle_{\chi_{\varphi^t}} = \frac{1}{A}\int_X \psi^t(x)\mathrm{d}\chi_{\varphi^t} = 0. \tag{2.28}$$

Additionally, for manifolds with (static) boundary, for which (2.16) holds, we have a boundary condition for ψ^t. Since the velocity w_T has the form (2.24), we have

$$g_\varphi(\nabla_{g_\varphi}\psi, \nu)|_{\partial X} = 0, \tag{2.29}$$

which is a natural Neumann boundary condition for ψ^t.

2.4. Elimination of a numerical tangential velocity

Our basic model is the mean curvature flow

$$\partial_t \varphi = h. \tag{2.30}$$

We can rewrite the model into the form

$$\begin{aligned} \partial_t\varphi \cdot N &= h \cdot N, \\ (\partial_t\varphi \cdot T_1)T_1 + (\partial_t\varphi \cdot T_2)T_2 &= 0, \end{aligned} \tag{2.31}$$

where T_1, T_2 are vectors tangent to the surface and the vectors T_1, T_2, N form an orthonormal basis at each point of the surface. From the analytical point of view, the forms (2.30) and (2.31) are equivalent, because

$$\partial_t\varphi = (\partial_t\varphi \cdot N)N + \sum_{i=1}^{2}(\partial_t\varphi \cdot T_i)T_i = (h \cdot N)N = HN = h.$$

The difference seems to be only formal: in the equations (2.31) the normal and (zero) tangential velocity is prescribed separately and in (2.30) we prescribe the total velocity vector $\partial_t\varphi$. However, the forms differ in the discrete setting. The mean curvature vector $h = HN$ is replaced by the Laplace–Beltrami operator $h = \triangle_\varphi\varphi$ and after discretization, the vector $\triangle_\varphi\varphi$ does not necessarily point in the normal direction, due to distretization errors. Using (2.31) we obtain

$$\partial_t\varphi = (\partial_t\varphi \cdot N)N + \sum_{i=1}^{2}(\partial_t\varphi \cdot T_i)T_i = (\triangle_\varphi\varphi \cdot N)N. \tag{2.32}$$

In equation (2.32) the total velocity vector $\partial_t\varphi$ necessarily points in the normal direction (regardless of the discretization), because the vector $\triangle_\varphi\varphi$ is projected onto the normal. Therefore, any tangential motion is prohibited. For a future reference in Section 4 we rewrite the model (2.32) by adding zero to the right-hand side

$$\begin{aligned}\partial_t\varphi &= \triangle_\varphi\varphi - \big(\triangle_\varphi\varphi - (\triangle_\varphi\varphi \cdot N)N\big)\\ &= \triangle_\varphi\varphi - \big(h - (h \cdot N)N\big).\end{aligned} \tag{2.33}$$

In the discrete setting, the term $\big(h - (h \cdot N)N\big)$ represents the numerical tangential velocity (if it is present).

3. Cotangent scheme and motivation for a new method

In this section we outline a discretization of the model (2.8) by a finite volume technique. The Laplace–Beltrami term is discerized by the broadly used cotangent scheme (see [25]).

To discretize the model (2.8) in the time domain, we apply a semi-implicit approach. The time derivative is approximated by a finite difference, and the Laplace–Beltrami operator and the tangential velocity are taken from the previous time step. If τ is the time step, $N = t_f/\tau$ is the number of time steps, $t^n = n\tau$ and $\varphi^n = \varphi(\cdot, t^n)$, we obtain

$$\frac{\varphi^n - \varphi^{n-1}}{\tau} = \triangle_{\varphi^{n-1}}\varphi^n + v_T^{n-1} \tag{3.1}$$

for $n = 1, \dots, N$, where the symbol $\triangle_{\varphi^{n-1}}$ denotes the Laplace–Beltrami operator from the previous time step with respect to the metric $g_{\varphi^{n-1}}$ induced by φ^{n-1}.

The space discretization is performed using a finite volume method. We consider a triangulation $\bar{X}$ of the manifold X, which is a simplical complex homeomorphic to X. Corresponding homeomorphism $\rho : \bar{X} \to X$ induces a triangular structure on X consisting of vertices $x_i = \rho(\bar{x}_i)$, $i = 1, \dots, n_F$, edges e_j, $j = 1, \dots, n_E$ and triangles $\mathcal{T}_p$, $p = 1, \dots, n_T$, where $\bar{x}_i$, $i = 1, \dots, n_F$ are the vertices of the triangulation $\bar{X}$.

The surface $X^n = \varphi^n(X)$ is also endowed with a triangular structure induced by the map $\varphi^n \circ \rho$ (Fig. 6, sketched by solid lines). We define an approximation of X^n using a new embedding $\bar{\varphi}^n : X \to \mathbb{R}^3$. For a triangle $\mathcal{T}_{i,p}$ with vertices $x_i, x_{i,p}, x_{i,p+1}$ we set

$$\bar{\varphi}^n(x) = (1 - \lambda - \mu)F_i^n + \lambda F_{i,p}^n + \mu F_{i,p+1}^n, \qquad x \in \mathcal{T}_{i,p}, \tag{3.2}$$

where $F_i^n = \varphi^n(x_i)$, $F_{i,p}^n = \varphi^n(x_{i,p})$ and $\lambda \in [0,1]$, $\mu \in [0, 1-\lambda]$ are the local coordinates of a point $x \in \mathcal{T}_{i,p}$ (Fig. 7, right). The surface $\bar{X}^n = \bar{\varphi}^n(X)$ is a polyhedral approximation of X^n (Fig. 6, sketched by dashed lines) with vertices $F_i^n = \varphi^n(x_i) = \bar{\varphi}^n(x_i)$, edges $e_j^n = \bar{\varphi}^n(e_j)$ and triangular faces $\mathcal{T}_p^n = \bar{\varphi}^n(\mathcal{T}_p)$.

The finite volume mesh (Fig. 8, *right*) is constructed by the barycentric subdivision of X. The finite volume (or covolume) V_i around a vertex x_i is a region bounded by the piecewise linear curve joining the barycenters $b_{i,p}$ of the neighbouring triangles and the midpoints $c_{i,p}$ of the edges leading to the neighbouring vertices $x_{i,p}$, $p = 1, \dots, m_i$ where m_i is the number of neighbours of the vertex $x_{i,p}$ (Fig. 7, *left*)[3]. The boundary edges of the covolume V_i are denoted by $\sigma_{i,p,1}$, $\sigma_{i,p,2}$, and the outward unit normals by $\nu_{i,p,1}$, $\nu_{i,p,2}$ respectively. For the sake of simplicity we omit the index i in most cases.

[3]The barycentric subdivision is effectively constructed on $\bar{X}^n$ and "pulled back" to X. In absence of the embedding $\bar{\varphi}^n : X \to \mathbb{R}^3$ and induced metric $g_{\bar{\varphi}^n} = \bar{\varphi}^{n*} g_Y$ (g_Y represents the standard Euclidean metric in $\mathbb{R}^3$), the notions as "piecewise linear curve" and "barycenter" would not have any meaning.

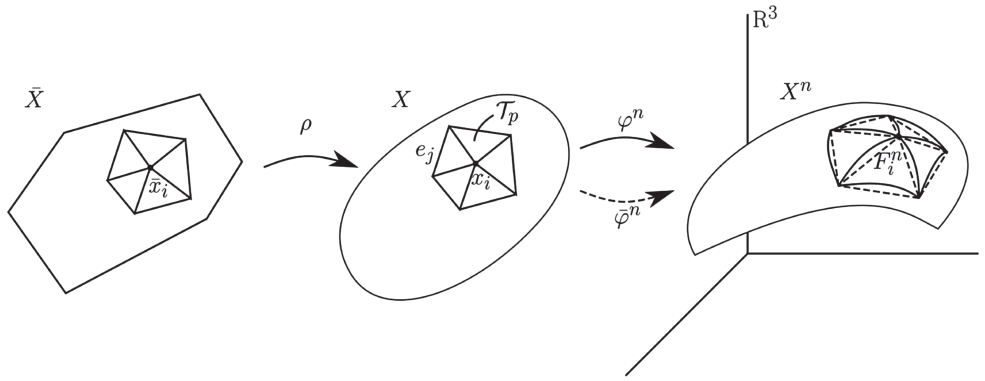

FIGURE 6. Triangulated surface from the point of view of the differential geometry (schematic sketch).

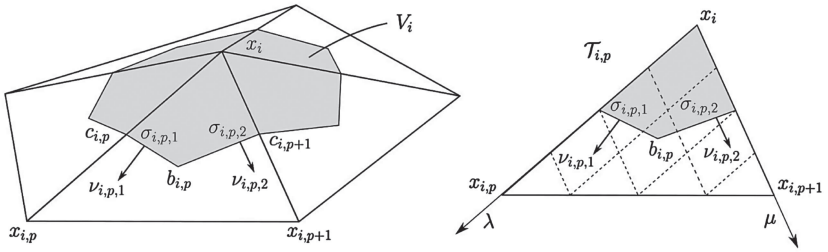

FIGURE 7. *Left panel*: the finite volume V_i around the vertex x_i. *Right panel*: the local coordinates on a triangle $\mathcal{T}_{i,p}$.

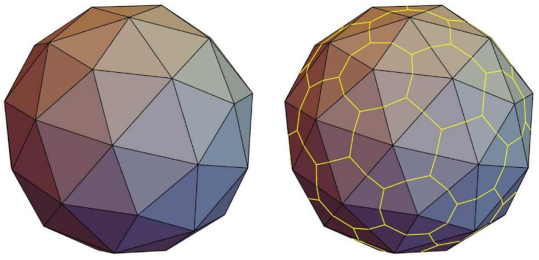

FIGURE 8. A discretization of the sphere S^2 embedded in $\mathbb{R}^3$. *Left panel*: the triangulation $\bar{X}^n$. *Right panel*: the triangulation $\bar{X}^n$ and the boundaries $\bar{\varphi}^n(\partial V_i)$ of the finite volumes $V_i, i = 1, \ldots, n_F$.

To obtain the equation for F_i^n, *i.e.* the position of the i-th vertex in n-th time step, we take the equation (3.1) with φ^n being replaced by its piecewise linear approximation $\bar{\varphi}^n$ and integrate it over a finite volume V_i. On the left-hand side we get

$$\int_{V_i} \frac{\bar{\varphi}^n - \bar{\varphi}^{n-1}}{\tau} \mathrm{d}\chi_{\bar{\varphi}^{n-1}} \approx A_i^{n-1} \frac{F_i^n - F_i^{n-1}}{\tau}, \tag{3.3}$$

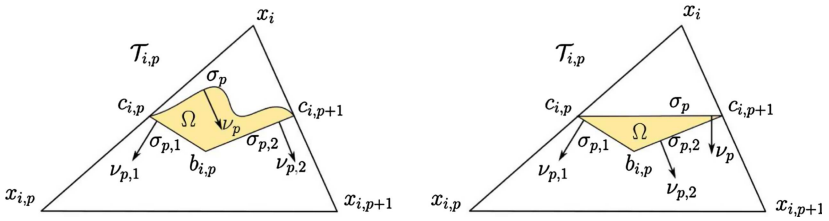

FIGURE 9. Path independence of the integral from $c_{i,p}$ to $c_{i,p+1}$.

where $\chi_{\bar\varphi^{n-1}}$ is the measure on X induced by the metric tensor $g_{\varphi^{n-1}}$ and $\bar\varphi^n(x)$ was approximated by its value in the vertex x_i, thus $\bar\varphi^n(x) \approx F_i^n$ for $x \in V_i$. The symbol $A_i^n \equiv \chi_{\bar\varphi^{n-1}}(V_i)$ denotes the area of the finite volume V_i. For the Laplace–Beltrami term on the right-hand side we have

$$\begin{aligned}\int_{V_i} \triangle_{\bar\varphi^{n-1}}\bar\varphi^n \,\mathrm{d}\chi_{\bar\varphi^{n-1}} &= \int_{\partial V_i} g_{\bar\varphi^{n-1}}\left(\nabla_{\bar\varphi^{n-1}}\bar\varphi^n, \nu_i^{n-1}\right)\,\mathrm{d}H_{\chi_{\bar\varphi^{n-1}}}\\ &= \sum_{p=1}^{m_i}\sum_{s=1,2}\int_{\sigma_{p,s}} g_{\bar\varphi^{n-1}}\left(\nabla_{\bar\varphi^{n-1}}\bar\varphi^n, \nu_{p,s}^{n-1}\right)\,\mathrm{d}H_{\chi_{\bar\varphi^{n-1}}},\end{aligned} \tag{3.4}$$

where $\nabla_{\bar\varphi^{n-1}}$ denotes the gradient with respect to the metric $g_{\bar\varphi^{n-1}}$, $\nu_{p,s}^{n-1}$ is the outward unit normal to $\sigma_{p,s}^{n-1}$ and $H_{\chi_{\bar\varphi^{n-1}}}$ is the Hausdorff measure on ∂V_i induced by $\chi_{\bar\varphi^{n-1}}$. Notice that since $\bar\varphi^n$ is piecewise linear, the gradient $\nabla_{\bar\varphi^{n-1}}\bar\varphi^n$ is constant on each $\mathcal{T}_{i,p}$. For the tangential velocity term we use the following approximation

$$\int_{V_i} v_T^{n-1}\,\mathrm{d}\chi_{\bar\varphi^{n-1}} \approx A_i^{n-1}\, v_{T,i}^{n-1}, \tag{3.5}$$

where $v_{T,i}^{n-1}$ is the tangential velocity of the vertex F_i^{n-1}.

3.1. Path independence of the integral from $c_{i,p}$ to $c_{i,p+1}$

We integrate $\triangle_{\bar\varphi^{n-1}}\bar\varphi^n$ over a region $\Omega \subset \mathcal{T}_{i,p}$, such that $\sigma_{p,1}, \sigma_{p,2} \subset \partial\Omega$ (see Fig. 9, *left*). Since the map $\bar\varphi^{n-1}$ is linear on $\mathcal{T}_{i,p}$ we have $\triangle_{\bar\varphi^{n-1}}\bar\varphi^n = 0$ and therefore (the index n is omitted)

$$\begin{aligned} 0 = \int_\Omega \triangle_{\bar\varphi}\bar\varphi\,\mathrm{d}\chi_{\bar\varphi} &= \int_{\partial\Omega} g_{\bar\varphi}\left(\nabla_{\bar\varphi}\bar\varphi, \nu\right)\,\mathrm{d}H_\chi\\ &= \sum_{s=1,2}\int_{\sigma_{p,s}} g_{\bar\varphi}\left(\nabla_{\bar\varphi}\bar\varphi, \nu_{p,s}\right)\,\mathrm{d}H_\chi + \int_{\sigma_p} g_{\bar\varphi}\left(\nabla_{\bar\varphi}\bar\varphi, -\nu_p\right)\,\mathrm{d}H_\chi,\end{aligned} \tag{3.6}$$

where $-\nu_p$ is the outward unit normal on σ_p (Fig. 9, *left*). The relation (3.6) implies

$$\sum_{s=1,2}\int_{\sigma_{p,s}} g_{\bar\varphi}\left(\nabla_{\bar\varphi}\bar\varphi, \nu_{p,s}\right)\,\mathrm{d}H_\chi = \int_{\sigma_p} g_{\bar\varphi}\left(\nabla_{\bar\varphi}\bar\varphi, \nu_p\right)\,\mathrm{d}H_\chi, \tag{3.7}$$

which means that we can replace the integration path $\sigma_{p,1}\cup\sigma_{p,2}$ by any other simple path connecting $c_{i,p}$ with $c_{i,p+1}$.

Consequently the integral (3.4) depends only on the position of the vertices $x_i, x_{i,p}, x_{i,p+1}$ of the triangle $\mathcal{T}_{i,p}$ and is independent of the exact shape of the path between the midpoints $c_{i,p}$, $c_{i,p+1}$. The point $b_{i,p}$ can be shifted anywhere inside $\mathcal{T}_{i,p}$ and the integral remains untouched. In the DDFV method we reduce this non-uniqueness by including the vertex $T_{i,p}^n = \bar\varphi^n(b_{i,p})$ to unknowns.

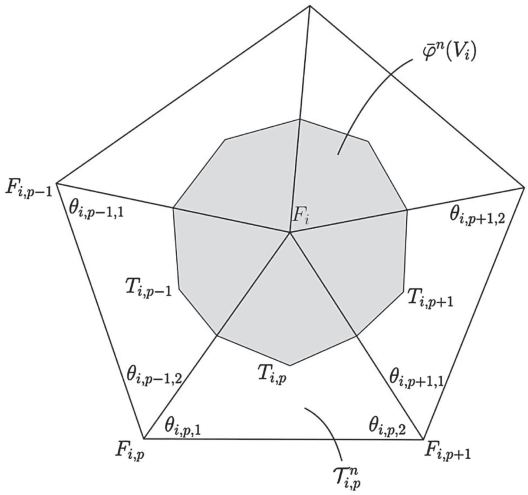

FIGURE 10. Notation around the vertex F_i.

3.2. Fully discrete formulation

If one calculates the integral in (3.4) (see, *e.g.*, [25] or [43] for details), one obtains a system

$$\mathfrak{a}_i^{n-1} F_i^n + \sum_{p=1}^{m_i} \mathfrak{b}_{i,p}^{n-1} F_{i,p}^n = F_i^{n-1} + \tau v_{T,i}^{n-1} \tag{3.8}$$

for $i = 1, \dots, n_F$ and $n = 1, \dots, N$, where

$$\begin{aligned} \mathfrak{a}_i^{n-1} &= 1 + \frac{\tau}{2A_i^{n-1}} \sum_{p=1}^{m_i} \left(\cot \theta_{i,p,1}^{n-1} + \cot \theta_{i,p,2}^{n-1} \right) \\ \mathfrak{b}_{i,p}^{n-1} &= -\frac{\tau}{2A_i^{n-1}} \left(\cot \theta_{i,p-1,1}^{n-1} + \cot \theta_{i,p,2}^{n-1} \right) \end{aligned} \tag{3.9}$$

for $p = 1, \dots, m_i$, where by convention $\theta_{i,0,1}^{n-1} = \theta_{i,m_i,1}^{n-1}$ (see Fig. 10 for the notation of the angles and vertices). A formula for the discrete tangential velocity $v_{T,i}^{n-1}$ is derived in [27,43]. In case of a surface with boundary, the Dirichlet boundary condition (2.2) is realized trivially by replacing the corresponding equations in the system (3.8) with

$$F_i^n = F_i^{n-1} \qquad \text{for each } F_i^n \in \partial \bar{X}^n. \tag{3.10}$$

In some cases the tangential motion along boundary may be desirable but, for simplicity, we fix the boundary points in this paper. The equations (3.8) (or (3.8) and (3.10) for surfaces with boundary) form a system of n_F linear equations for the unknowns F_i^n, $i = 1, \dots, n_F$. The initial positions of the vertices F_i^0 are given by the initial condition, *i.e.* $F_i^0 = F^0(x_i)$.

4. Discrete duality finite volume method

In this section we present a Discrete duality finite volume (DDFV) method for solving mean curvature flow (model (2.8)). We provide the method with a suitable area-oriented tangential redistribution.

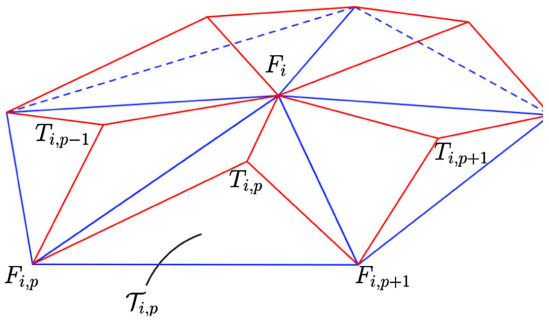

FIGURE 11. The edges of the original mesh (*blue lines*) and the edges of the diamond mesh (*red lines*) in the neighbourhood of the vertex F_i (Color online).

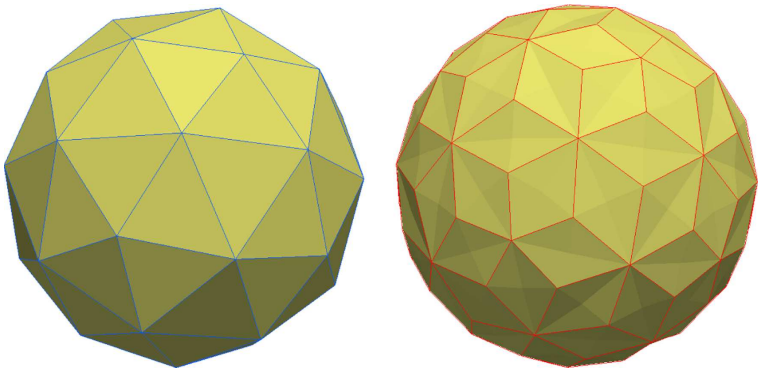

FIGURE 12. The discretization of the sphere S^2 embedded in $\mathbb{R}^3$. *Left panel*: the triangular mesh $\bar{X}^n$ for the cotangent scheme. *Right panel*: the diamond mesh $\bar{X}^n$ for the DDFV method.

4.1. Discretization of the mean curvature flow

To discretize the model (2.8) in the time domain we adopt the semi-implicit approach from Section 3, *i.e.* we use the discretization (3.1). The space discretization is described in the following sections.

4.1.1. Diamond mesh

In our approach we modify the triangular mesh $\bar{X}^n$ introduced in Section 3. We create a representative point T_i^n of each triangle $\mathcal{T}_i^n$ (Fig. 11). The point T_i^n does not need to lie in the triangle, only its projection to the hyperplane containing the triangle $\mathcal{T}_i^n$ does.

The vertices $F_i^n, i = 1, \dots n_F$ and $T_i^n, i = 1, \dots n_T$ will be referred to as F-vertices and T-vertices respectively. Next, the triangular mesh is replaced by a diamond mesh which is constructed as follows. The edges of the diamond mesh (see Figs. 11 and 12, *right*) are the line segments joining each F-vertex with all neighbouring T-vertices (*i.e.* the representative points of the former neighbouring triangular faces). For a manifold with boundary, the edges connecting boundary F-vertices are also included to the diamond mesh (Fig. 13, *right*). The basic geometric object is a diamond cell, denoted by V^D, which is a surface patch bounded by four edges (Fig. 14). For a manifold with boundary, the boundary diamond cells V^D are triangles with two F-vertices and one T-vertex (Fig. 13, *right*).

The manifold $\bar{X}$ and the homeomorphism $\rho : \bar{X} \to X$ are changed analogously. The homeomorphism ρ induces a new structure on X with vertices x_i, $i = 1, \dots, n_F$ and b_i, $i = 1, \dots, n_T$. For the embedding $\bar{\varphi}^n : X \to \mathbb{R}^3$ of

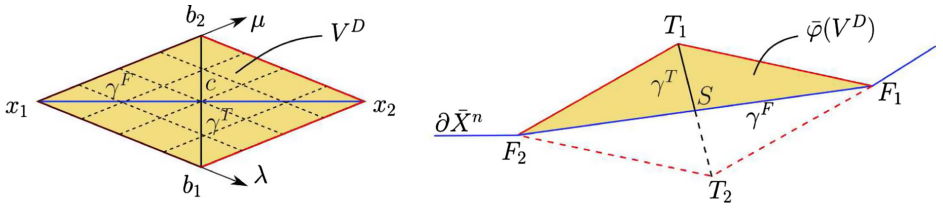

FIGURE 13. *Left panel*: the local coordinates on an inner diamond cell on X. *Right panel*: a boundary diamond cell on $\bar{X}^n$.

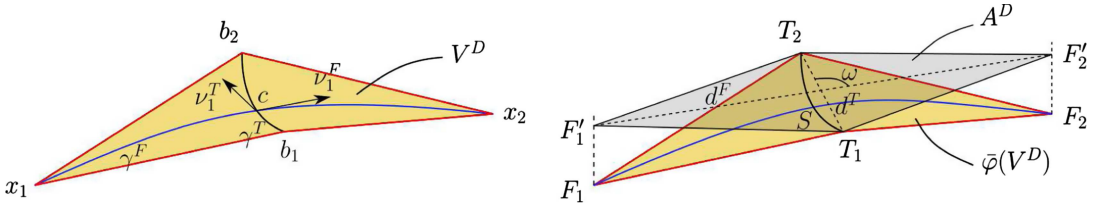

FIGURE 14. The geometry of a diamond cell. *Left panel*: a diamond cell on the manifold X. *Right panel*: $\bar{\varphi}$-image of a diamond cell on $\bar{X}^n$.

a diamond cell V^D with vertices x_1, b_1, x_2, b_2 we use a bilinear interpolation

$$\bar{\varphi}^n(x) = (1-\lambda)(1-\mu)F_1^n + \lambda\mu F_2^n + \lambda(1-\mu)T_1^n + (1-\lambda)\mu T_2^n, \qquad x \in V^D, \tag{4.1}$$

where $T_i^n = \varphi^n(b_i)$, $F_i^n = \varphi^n(x_i)$ and $\lambda, \mu \in [0,1]$ are the local coordinates of a point $x \in V^D$ (Fig. 13, *left*). The quantities needed in following computations are denoted in Fig. 14 and will be defined properly later. The center c of an inner diamond cell V^D is defined by $\bar{\varphi}^n(c) = \frac{1}{4}(F_1^n + T_1^n + F_2^n + T_2^n) = S$.

If V^D is a boundary diamond cell with vertices x_1, b_1, x_2 we use a linear interpolation

$$\bar{\varphi}^n(x) = (1-\lambda)F_1^n + \mu F_2^n + (\lambda-\mu)T_1^n, \qquad x \in V^D, \tag{4.2}$$

where $\lambda \in [0,1]$ and $\mu \in [0,\lambda]$. We obtained (4.2) from (4.1) by replacing T_2 with a point reflection of T_1 with respect to $S = \frac{1}{2}(F_1 + F_2)$ (Fig. 13, *right*).

$$T_2 = T_1 + 2(S - T_1) = F_1 + F_2 - T_1. \tag{4.3}$$

The resulting mesh consists of $n_V = n_F + n_T$ vertices and n_{dia} diamond cells[4]. Our diamond mesh is a generalization of 2D planar diamond mesh used in discrete duality finite volume method developed in [11] (see also [10]) to 2D surfaces in $\mathbb{R}^3$.

Induced metric $g_{\bar{\varphi}^n}$ and surface normal. In following we will need an expression for induced metric $g_{\bar{\varphi}^n} = (\bar{\varphi}^n)^* g_Y$ in the center of a diamond cell V^D. The standard Euclidean metric tensor in $\mathbb{R}^3$ is

$$g_Y = dx \otimes dx + dy \otimes dy + dz \otimes dz, \tag{4.4}$$

where (x, y, z) are Cartesian coordinates in $\mathbb{R}^3$. The pull back of (4.4) from $\mathbb{R}^3$ by the map $\bar{\varphi}$ reads (in the matrix form)

$$g_{\bar{\varphi}^n} \leftrightarrow [g_{ab}(\lambda,\mu)] = \begin{pmatrix} \|(1-\mu)u_1 + \mu u_2\|^2 & f(\lambda,\mu) \\ f(\lambda,\mu) & \|(1-\lambda)v_1 + \lambda v_2\|^2 \end{pmatrix}, \tag{4.5}$$

[4]In case of a closed manifold $n_{\text{dia}} = \frac{3}{2}n_T$. For a manifold with boundary $n_{\text{dia}} > \frac{3}{2}n_T$ and n_{dia} approaches $\frac{3}{2}n_T$ with refinement of the mesh.

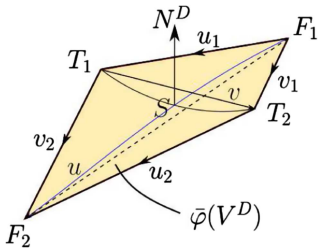

FIGURE 15. A diamond cell in $\mathbb{R}^3$.

where $u_1 = T_1 - F_1$, $u_2 = F_2 - T_2$, $v_1 = T_2 - F_1$, $v_2 = F_2 - T_1$ (Fig. 15) and

$$f(\lambda,\mu) = (1-\lambda a)(1-\mu)(u_1\cdot v_1) + \lambda\mu(u_2\cdot v_2) + \lambda(1-\mu)(u_1\cdot v_2) + (1-\lambda)\mu(u_2\cdot v_1).$$

In the center c which is a point with coordinates $(\lambda,\mu) = \left(\frac{1}{2},\frac{1}{2}\right)$ we have

$$g^c_{\bar{\varphi}^n} \leftrightarrow \left[g_{ab}\left(\tfrac{1}{2},\tfrac{1}{2}\right)\right] = \frac{1}{4}\begin{pmatrix} \|u_1+u_2\|^2 & (u_1+u_2)\cdot(v_1+v_2) \\ (u_1+u_2)\cdot(v_1+v_2) & \|v_1+v_2\|^2 \end{pmatrix}, \tag{4.6}$$

which can be rewritten using the notation $u = F_2 - F_1$, $v = T_2 - T_1$ (Fig. 15) to the form

$$g^c_{\bar{\varphi}^n} \leftrightarrow \left[g_{ab}\left(\tfrac{1}{2},\tfrac{1}{2}\right)\right] = \frac{1}{4}\begin{pmatrix} \|u-v\|^2 & (u-v)\cdot(u+v) \\ (u-v)\cdot(u+v) & \|u+v\|^2 \end{pmatrix}. \tag{4.7}$$

For a future reference we state the expression for the surface normal in the middle of the diamond cell (Fig. 15)

$$N^D = \frac{u\times v}{\|u\times v\|}, \qquad \text{with} \qquad u = F_2 - F_1, \quad v = T_2 - T_1. \tag{4.8}$$

4.1.2. Finite volumes

Since we have two types of vertices: F- and T-vertices, we need two types of finite volumes over which we will integrate the equation (3.1) to obtain the system of linear equations for unknowns $F_i^n, i = 1,\dots n_F$ and $T_i^n, i = 1,\dots n_T$.

Finite volume for F-vertex. A finite volume V_i^F around a vertex x_i is a region bounded by a curve joining the neighbouring vertices $b_{i,p}$ and the centers $c_{i,p}$ of the diamond cells $V^D_{i,p}$, $p = 1,\dots,m_i$ (for the notation see Fig. 17, *left*, see also Fig. 16, *left*). The part of the boundary between $b_{i,p-1}$ and $b_{i,p}$ is a curve $\gamma^T_{i,p}$ given by the coordinate expression (by convention, x_i is the origin of the local coordinate system on each $V^D_{i,p}$)

$$\gamma^T_{i,p}: \qquad (\lambda(t),\mu(t)) = (1-t,t), \qquad t\in[0,1]. \tag{4.9}$$

The area $A_i^{F,n} = \chi_{\bar{\varphi}^n}(V_i^F)$ of a finite volume V_i^F is approximated by the total area of $2m_i$ triangles with vertices $F_i^n, S^n_{i,p}, T^n_{i,p}$ and $F_i^n, T^n_{i,p}, S^n_{i,p+1}$ (Fig. 17, *right*) for $p = 1,\dots,m_i$ (by convention, $S^n_{i,m_i+1} = S^n_{i,1}$). These triangles are used for visualisation in Figure 16 and throughout the whole section.

The surface normal N_i^F in the vertex F_i^n is approximated by the normalized average of the surface normals $N^D_{i,p}$ to the neighbouring diamond cells $V^D_{i,p}$ (calculated using (4.8))

$$N_i^F = \frac{\hat{N}_i^F}{\|\hat{N}_i^F\|}, \qquad \text{where} \qquad \hat{N}_i^F = \frac{1}{m_i}\sum_{p=1}^{m_i} N^D_{i,p}. \tag{4.10}$$

The normalization is necessary because the average $\hat{N}_i^F$ is not a unit vector in general.

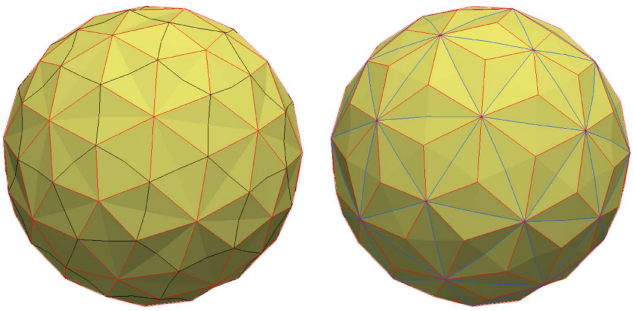

FIGURE 16. *Left panel*: the diamond mesh with boundaries of the covolumes for F-vertices. *Right panel*: the diamond mesh with boundaries of the covolumes for T-vertices.

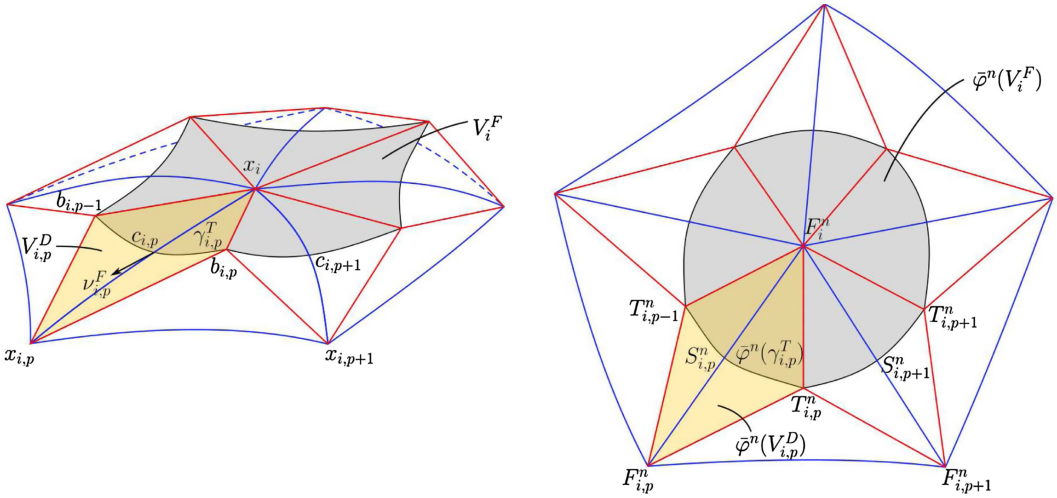

FIGURE 17. *Left panel*: the finite volume V_i^F around a vertex $x_i \in X$. *Right panel*: the notation in the neighbourhood of a vertex $F_i^n = \bar{\varphi}^n(x_i) \in \bar{X}^n$.

Finite volume for T-vertex. We construct a finite volume V_i^T (Figs. 18, *left* and 16, *right*) around the vertex b_i as a region bounded by the curves $\gamma_{i,p}^F$, $p = 1, 2, 3$ given by the coordinate expression (by convention, the point $x_{i+1,p}$ is the origin of the local coordinate system on each $V_{i,p}^D$)

$$\gamma_{i,p}^F : \qquad (\lambda(t), \mu(t)) = (1-t, 1-t), \qquad t \in [0,1]. \tag{4.11}$$

The area $A_i^{T,n} = \chi_{\bar{\varphi}^n}(V_i^T)$ of the covolume V_i^T is approximated by the total area of 6 triangles with vertices $T_i^n, F_{i,p}^n, S_{i,p}^n$ and $T_i^n, S_{i,p}^n, F_{i,p+1}^n$ (Fig. 18, *right*) for $p = 1, 2, 3$ (by convention, $F_{i,4}^n = F_{i,1}^n$).

The surface normal N_i^T in the vertex T_i is approximated analogously to (4.10) as

$$N_i^T = \frac{\hat{N}_i^T}{\|\hat{N}_i^T\|}, \qquad \text{where} \qquad \hat{N}_i^T = \frac{1}{3}\sum_{p=1}^{3} N_{i,p}^D. \tag{4.12}$$

4.1.3. Integration over finite volumes

To obtain the equation for F_i^n we integrate (3.1) over V_i^F, with φ^n being replaced by its piecewise bilinear approximation $\bar{\varphi}^n$. By the same procedure as in the Section 3 we obtain (using analogues of (3.3), (3.4) and (3.5))

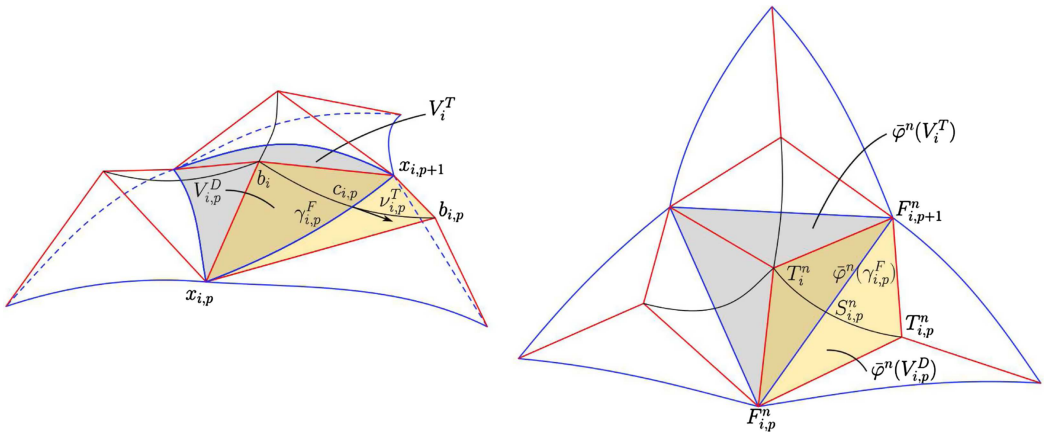

FIGURE 18. *Left panel*: the finite volume V_i^T around the vertex $b_i \in X$. *Right panel*: the notation around of the vertex $T_i^n = \bar\varphi^n(b_i) \in \bar X^n$.

$$A_i^{F,n-1}\frac{F_i^n - F_i^{n-1}}{\tau} = \sum_{p=1}^{m_i} \int_{\gamma_{i,p}^T} g_{\bar\varphi^{n-1}}\left(\nabla_{\bar\varphi^{n-1}}\bar\varphi^n, \nu_{i,p}^{n-1}\right) \mathrm{d}H_{\chi_{\bar\varphi^{n-1}}} + A_i^{F,n-1} v_{T,i}^{F,n-1}, \tag{4.13}$$

where $\nu_{i,p}^{n-1}$ is the outward unit normal to the covolume V_i^F on the curve $\gamma_{i,p}^T$ and $v_{T,i}^{F,n-1}$ is a tangential velocity of the vertex F_i^n. For a vertex T_i^n we integrate the formula (3.1) over V_i^T and obtain formula analogous to (4.13)

$$A_i^{T,n-1}\frac{T_i^n - T_i^{n-1}}{\tau} = \sum_{p=1}^{3} \int_{\gamma_{i,p}^F} g_{\bar\varphi^{n-1}}\left(\nabla_{\bar\varphi^{n-1}}\bar\varphi^n, \nu_{i,p}^{n-1}\right) \mathrm{d}H_{\chi_{\bar\varphi^{n-1}}} + A_i^{T,n-1} v_{T,i}^{T,n-1}. \tag{4.14}$$

The formulas (4.13) and (4.14) are analogous to the cotangent scheme but the computation of the integrals on right-hand side will differ. We compute the integrals in the following sections (a non-interested reader can easily skip to the Sect. 4.1.4). The computation of the tangential velocities $v_{T,i}^{F,n-1}$ and $v_{T,i}^{T,n-1}$ is in Section 4.2.

Calculation of the integral over $\boldsymbol{\gamma_{i,p}^T}$. We approximate the value of the integral in (4.13) using the value in the center $c_{i,p}$. To simplify the notation we omit most of the indices i and n throughout this section.

$$\int_{\gamma_p^T} g_{\bar\varphi}\left(\nabla_{\bar\varphi}\bar\varphi, \nu_p\right) \mathrm{d}H_\chi \approx \left|\gamma_p^T\right| g_{\bar\varphi}^{c_p}\left(\nabla_{\bar\varphi}\bar\varphi(c_p), \nu_p^F\right), \tag{4.15}$$

where $|\gamma_p^T| = \|T_{p-1} - S_p\| + \|T_i - S_p\|$ is the approximate length of the curve γ_p^T and $\nu_p^F = \nu_p(c_p)$ is the outward unit normal to ∂V_i^F at the point c_p. The tangent vector to γ_p^T at point c_p is $\dot\gamma_p^T = -\partial_\lambda + \partial_\mu$ (see the definition (4.9)). We obtain a formula for the normal $\nu_p^F = (\nu_p^F)^\lambda \partial_\lambda + (\nu_p^F)^\mu \partial_\mu$ after using conditions $g_{\bar\varphi}^{c_p}(\dot\gamma_p^T, \nu_p^F) = 0$ (orthogonality), $g_{\bar\varphi}^{c_p}(\nu_p^F, \nu_p^F) = 1$ (normalization) and $(\nu_p^F)^\lambda, (\nu_p^F)^\mu > 0$ (correct orientation) in the following form

$$\nu_p^F = \frac{\|v\|^2 + u\cdot v}{\|v\|\sqrt{\|u\|^2\|v\|^2 - (u\cdot v)^2}}\partial_\lambda + \frac{\|v\|^2 - u\cdot v}{\|v\|\sqrt{\|u\|^2\|v\|^2 - (u\cdot v)^2}}\partial_\mu, \tag{4.16}$$

where $u = F_{i,p} - F_i$, $v = T_{i,p} - T_{i,p-1}$. Now we evaluate the derivatives of the embedding (4.1) in the center c_p of the diamond cell

$$\partial_\lambda\bar\varphi(c_p) = \frac{1}{2}(u - v), \qquad \partial_\mu\bar\varphi(c_p) = \frac{1}{2}(u + v). \tag{4.17}$$

Let g_{ab} denote the components (4.6) of the metric $g_{\bar\varphi}$ and g^{ab} the components of the inverse matrix. Then $\nabla_{\bar\varphi}\bar\varphi = \sum_{a,c=1,2} g^{ac}(\partial_c\bar\varphi)\partial_a$ and $\nu_p = \sum_{b=1,2} \nu_p^b\partial_b$ and their inner product is

$$g_{\bar\varphi}\left(\nabla_{\bar\varphi}\bar\varphi, \nu_p\right) = \sum_{a,b,c=1,2} g_{ab}g^{ac}(\partial_c\bar\varphi)\nu_p^b = \sum_{b,c=1,2} \delta_b^c(\partial_c\bar\varphi)\nu_p^b = \sum_{b=1,2} \nu_p^b\partial_b\bar\varphi. \tag{4.18}$$

Using (4.16)–(4.18) we calculate the integral (4.15) as follows

$$\begin{aligned}
\int_{\gamma_p^T} g_{\bar\varphi}\left(\nabla_{\bar\varphi}\bar\varphi, \nu_p\right) \mathrm{d}H_\chi &= \frac{\left|\gamma_p^T\right|}{2}\left((\nu_p^F)^\lambda(u-v) + (\nu_p^F)^\mu(u+v)\right) \\
&= \frac{\left|\gamma_p^T\right|}{2}\left[\left((\nu_p^F)^\lambda + (\nu_p^F)^\mu\right)u + \left((\nu_p^F)^\mu - (\nu_p^F)^\lambda\right)v\right] \\
&= \frac{\left|\gamma_p^T\right|\|v\|}{\sqrt{\|u\|^2\|v\|^2 - (u\cdot v)^2}}u - \frac{\left|\gamma_p^T\right|u\cdot v}{\|v\|\sqrt{\|u\|^2\|v\|^2 - (u\cdot v)^2}}v \\
&= \frac{\left|\gamma_p^T\right|d_p^T}{2A_p^D}(F_{i,p} - F_i) - \frac{\left|\gamma_p^T\right|}{d_p^T}\cot\omega_p(T_{i,p} - T_{i,p-1}),
\end{aligned} \tag{4.19}$$

where $d_p^T = \|T_{i,p} - T_{i,p-1}\|$ is the euclidean distance between T-vertices of the diamond cell $V_{i,p}^D$. The area $A_p^D = \frac{1}{2}\sqrt{\|u\|^2\|v\|^2 - (u\cdot v)^2} = \frac{1}{2}\|u\times v\|$ can be interpreted as the approximate measure of the diamond cell calculated as the area of the quadrangle with vertices F_1', T_1, F_2', T_2 (Fig. 14, *right*) which we get by shifting the line segment F_1F_2 in the direction of the vector $u\times v$ until it intersects the segment T_1T_2 and ω_p is the angle between $F_1'F_2'$ and T_1T_2.

For a future reference in Section 4.2 we state a formula for the pushforward $\bar\varphi_*\nu_p^F$ of the normal ν_p^F. Pushforwards of the basis vectors $\partial_\lambda, \partial_\mu$ read $\bar\varphi_*\partial_\lambda = \partial_\lambda\bar\varphi = \frac{1}{2}(u-v)$ and $\bar\varphi_*\partial_\mu = \partial_\mu\bar\varphi = \frac{1}{2}(u+v)$, therefore

$$\bar\varphi_*\nu_p^F = \frac{\|v\|}{\sqrt{\|u\|^2\|v\|^2 - (u\cdot v)^2}}u - \frac{u\cdot v}{\|v\|\sqrt{\|u\|^2\|v\|^2 - (u\cdot v)^2}}v, \tag{4.20}$$

where $u = F_{i,p} - F_i$ and $v = T_{i,p} - T_{i,p-1}$.

Calculation of the integral over $\boldsymbol{\gamma_{i,p}^F}$. The computation is analogous to previous section, therefore we skip some details. The integral in (4.14) is approximated as (indices i, n omitted)

$$\int_{\gamma_p^F} g_{\bar\varphi}\left(\nabla_{\bar\varphi}\bar\varphi, \nu_p\right) \mathrm{d}H_\chi \approx \left|\gamma_p^F\right| g_{\bar\varphi}^{c_p}\left(\nabla_{\bar\varphi}\bar\varphi(c_p), \nu_p^T\right), \tag{4.21}$$

where $|\gamma_p^F| = \|F_p - S_p\| + \|F_{p+1} - S_p\|$ is the approximate length of γ_p^F and $\nu_p^T = \nu_p(c_p)$. The formula for the outward unit normal to V_i^T at c_p is

$$\nu_p^T = -\frac{\|u\|^2 + u\cdot v}{\|u\|\sqrt{\|u\|^2\|v\|^2 - (u\cdot v)^2}}\partial_\lambda + \frac{\|u\|^2 - u\cdot v}{\|u\|\sqrt{\|u\|^2\|v\|^2 - (u\cdot v)^2}}\partial_\mu, \tag{4.22}$$

where $u = F_{i,p} - F_{i,p+1}$, $v = T_{i,p} - T_i$. The integral over γ_p^F follows

$$\begin{aligned}\int_{\gamma_p^F} g_{\bar\varphi}\left(\nabla_{\bar\varphi}\bar\varphi, \nu_p\right) \mathrm{d}H_\chi &= \frac{\left|\gamma_p^F\right|}{2}\left[\left((\nu_p^T)^\mu - (\nu_p^T)^\lambda\right)v + \left((\nu_p^T)^\lambda + (\nu_p^T)^\mu\right)u\right] \\ &= \frac{\left|\gamma_p^F\right| \|u\|}{\sqrt{\|u\|^2\|v\|^2 - (u\cdot v)^2}}v - \frac{\left|\gamma_p^F\right| u\cdot v}{\|u\|\sqrt{\|u\|^2\|v\|^2 - (u\cdot v)^2}}u \\ &= \frac{\left|\gamma_p^F\right| d_p^F}{2A_p^D}(T_{i,p} - T_i) - \frac{\left|\gamma_p^F\right|}{d_p^F}\cot\omega_p(F_{i,p} - F_{i,p+1}),\end{aligned} \tag{4.23}$$

where $d_p^F = \|F_{i,p+1} - F_{i,p}\|$ is the euclidean distance between F-vertices of diamond cell $V_{i,p}^D$.

For a future reference in Section 4.2 we state a formula for the pushforward $\bar\varphi_*\nu_p^T$ of the normal ν_p^T

$$\bar\varphi_*\nu_p^T = -\frac{u\cdot v}{\|u\|\sqrt{\|u\|^2\|v\|^2 - (u\cdot v)^2}}u + \frac{\|u\|}{\sqrt{\|u\|^2\|v\|^2 - (u\cdot v)^2}}v, \tag{4.24}$$

where $u = F_{i,p} - F_{i,p+1}$ and $v = T_{i,p} - T_i$.

Approximation of the Laplace–Beltrami operator and the mean curvature. To obtain the discretization of the Laplace–Beltrami operator on a finite volume V_i^F we sum the integrals (4.19) over $p = 1, \dots, m_i$ and reorder the sum (replace p by $(p+1)$ in the term containing $T_{i,p-1}$). The final formula reads

$$\begin{aligned}\int_{V_i^F} \triangle_{\bar\varphi}\bar\varphi \,\mathrm{d}\chi_{\bar\varphi} &= \sum_{p=1}^{m_i}\int_{\gamma_{i,p}^T} g_{\bar\varphi}\left(\nabla_{\bar\varphi}\bar\varphi, \nu_{i,p}\right)\mathrm{d}H_\chi \\ &= -\frac{1}{2}\sum_{p=1}^{m_i}\frac{\left|\gamma_{i,p}^T\right| d_{i,p}^T}{A_{i,p}^D}F_i + \frac{1}{2}\sum_{p=1}^{m_i}\frac{\left|\gamma_{i,p}^T\right| d_{i,p}^T}{A_{i,p}^D}F_{i,p} \\ &\quad - \sum_{p=1}^{m_i}\left(\frac{\left|\gamma_{i,p}^T\right|}{d_{i,p}^T}\cot\omega_{i,p} - \frac{\left|\gamma_{i,p+1}^T\right|}{d_{i,p+1}^T}\cot\omega_{i,p+1}\right)T_{i,p}.\end{aligned} \tag{4.25}$$

Analogously we reorder (replace p by $(p-1)$ in the term containing $F_{i,p+1}$) the sum of integrals (4.23) over $p = 1, 2, 3$ to obtain discretization on a finite volume V_i^T

$$\begin{aligned}\int_{V_i^T} \triangle_{\bar\varphi}\bar\varphi \,\mathrm{d}\chi_{\bar\varphi} &= \sum_{p=1}^{3}\int_{\gamma_{i,p}^F} g_{\bar\varphi}\left(\nabla_{\bar\varphi}\bar\varphi, \nu_{i,p}\right)\mathrm{d}H_\chi \\ &= -\frac{1}{2}\sum_{p=1}^{3}\frac{\left|\gamma_{i,p}^F\right| d_{i,p}^F}{A_{i,p}^D}T_i + \frac{1}{2}\sum_{p=1}^{3}\frac{\left|\gamma_{i,p}^F\right| d_{i,p}^F}{A_{i,p}^D}T_{i,p} \\ &\quad - \sum_{p=1}^{3}\left(\frac{\left|\gamma_{i,p}^F\right|}{d_{i,p}^F}\cot\omega_{i,p} - \frac{\left|\gamma_{i,p-1}^F\right|}{d_{i,p-1}^F}\cot\omega_{i,p-1}\right)F_{i,p}.\end{aligned} \tag{4.26}$$

The formulas (4.25) and (4.26) can be used to express the discrete mean curvature vectors h_i^F and h_i^T at points F_i and T_i respectively. Since (2.6) holds, we have

$$h_i^F \approx \frac{1}{A_i^F} \int\limits_{V_i^F} \triangle_{\bar\varphi}\bar\varphi \, \mathrm{d}\chi_{\bar\varphi} = \frac{1}{2A_i^F} \left(\sum_{p=1}^{m_i} q_{i,p}^{FF}(F_{i,p} - F_i) - 2\sum_{p=1}^{m_i} q_{i,p}^{FT}(T_{i,p} - T_{i,p-1}) \right), \tag{4.27}$$

$$h_i^T \approx \frac{1}{A_i^T} \int\limits_{V_i^T} \triangle_{\bar\varphi}\bar\varphi \, \mathrm{d}\chi_{\bar\varphi} = \frac{1}{2A_i^T} \left(\sum_{p=1}^{3} q_{i,p}^{TT}(T_{i,p} - T_i) - 2\sum_{p=1}^{3} q_{i,p}^{TF}(F_{i,p} - F_{i,p+1}) \right). \tag{4.28}$$

The mean curvatures are approximated as

$$H_i^F = h_i^F \cdot N_i^F, \qquad H_i^T = h_i^T \cdot N_i^T, \tag{4.29}$$

with N_i^F and N_i^T denoting the surface normals at the points F_i and T_i respectively, given by (4.10) and (4.12). The average mean curvatures are computed as

$$\bar H_i^F = \frac{1}{A}\sum_{i=1}^{n_F} H_i^F A_i^F, \qquad \bar H_i^T = \frac{1}{A}\sum_{i=1}^{n_T} H_i^T A_i^T, \tag{4.30}$$

then $\bar h_i^F = \bar H_i^F N_i^F$ and $\bar h_i^T = \bar H_i^T N_i^T$. The total area A of the surface in (4.30) is given by

$$A = \sum_{i=1}^{n_F} A_i^F = \sum_{i=1}^{n_T} A_i^T. \tag{4.31}$$

4.1.4. Final equations

Equations for *F*-vertices. We combine (4.13) with (4.25) to obtain the equations for F-vertices in the form

$$\mathfrak{a}_i^{F,n-1} F_i^n + \sum_{p=1}^{m_i} \mathfrak{b}_{i,p}^{F,n-1} F_{i,p}^n + \sum_{p=1}^{m_i} \mathfrak{c}_{i,p}^{F,n-1} T_{i,p}^n = F_i^{n-1} + \tau v_{T,i}^{F,n-1} \tag{4.32}$$

for $i = 1, \dots, n_F$ and $n = 1, \dots, N$, where

$$\begin{aligned} \mathfrak{a}_i^F &= 1 + \frac{\tau}{2A_i^F}\sum_{p=1}^{m_i} q_{i,p}^{FF} \\ \mathfrak{b}_{i,p}^F &= -\frac{\tau}{2A_i^F} q_{i,p}^{FF} \\ \mathfrak{c}_{i,p}^F &= \frac{\tau}{A_i^F}\left(q_{i,p}^{FT} - q_{i,p+1}^{FT}\right) \end{aligned} \tag{4.33}$$

for $p = 1, \dots, m_i$, with $q_{i,m+1}^{FT} = q_{i,1}^{FT}$ and where

$$q_{i,p}^{FF} = \frac{|\gamma_{i,p}^T|\, d_{i,p}^T}{A_{i,p}^D}, \qquad q_{i,p}^{FT} = \frac{|\gamma_{i,p}^T|}{d_{i,p}^T}\cot\omega_{i,p}. \tag{4.34}$$

To reduce complexity of the notation we omitted the time step index n in (4.33) and (4.34). All geometric quantities in (4.33) and (4.34) are calculated from the $(n-1)$-th time step. In case of a surface with boundary, the Dirichlet boundary condition (2.2) is realized trivially by replacing the corresponding equations in (4.32) with

$$F_i^n = F_i^{n-1} \qquad \text{for each } F_i^n \in \partial\bar X^n. \tag{4.35}$$

Equations for T-vertices. To obtain the equations for T-vertices we use (4.26) in (4.14). The resulting formula is

$$\mathfrak{a}_i^{T,n-1} T_i^n + \sum_{p=1}^{3} \mathfrak{b}_{i,p}^{T,n-1} T_{i,p}^n + \sum_{p=1}^{3} \mathfrak{c}_{i,p}^{T,n-1} F_{i,p}^n = T_i^{n-1} + \tau v_{T,i}^{T,n-1} \tag{4.36}$$

for $i = 1, \dots, n_T$ and $n = 1, \dots, N$, where

$$\begin{aligned} \mathfrak{a}_i^T &= 1 + \frac{\tau}{2A_i^T} \sum_{p=1}^{3} q_{i,p}^{TT} \\ \mathfrak{b}_{i,p}^T &= -\frac{\tau}{2A_i^T} q_{i,p}^{TT} \\ \mathfrak{c}_{i,p}^T &= \frac{\tau}{A_i^T} \left(q_{i,p}^{TF} - q_{i,p-1}^{TF} \right) \end{aligned} \tag{4.37}$$

for $p = 1, 2, 3$, with $q_{i,0}^{TF} = q_{i,3}^{TF}$ and where

$$q_{i,p}^{TT} = \frac{\left|\gamma_{i,p}^F\right| d_{i,p}^F}{A_{i,p}^D}, \qquad q_{i,p}^{TF} = \frac{\left|\gamma_{i,p}^F\right|}{d_{i,p}^F} \cot \omega_{i,p}. \tag{4.38}$$

We omitted the index n in (4.37) and (4.38). All geometric quantities in (4.37) and (4.38) are calculated from the $(n-1)$th time step.

If a neighbouring diamond cell $V_{i,p}^D$ is a boundary diamond cell (Fig. 13, *right*), we perform a substitution (see Eq. (4.3))

$$T_{i,p}^n = F_{i,p}^n + F_{i,p+1}^n - T_i^n \tag{4.39}$$

in equation (4.36). The area $A_{i,p}^D$ is calculated as the area of the quadrangle with vertices $T_i^n, F_{i,p}, T_{i,p}^n, F_{i,p+1}^n$ with $T_{i,p}^n$ constructed by (4.39). Notice that in case of the boundary diamond cell $\left|\gamma_{i,p}^F\right| = d_{i,p}^F$ holds, therefore the formulas (4.38) can be simplified.

The formulas (4.32), (4.36) represent the system of $n_V = n_F + n_T$ linear equations for the unknowns F_i^n, $i = 1, \dots, n_F$ and T_i^n, $i = 1, \dots, n_T$. The system is coupled with an initial condition $F_i^0 = \varphi^0(x_i)$ and $T_i^0 = \varphi^0(b_i)$. If the initial positions of T-vertices are not provided, we can place $T_i^0, i = 1, \cdots, n_T$ to barycenters or use a procedure described on the page 4.2. The linear system can be represented by a matrix. For rows of the matrix it holds

$$\begin{aligned} \mathfrak{a}_i^{F,n-1} &= 1 - \sum_{p=1}^{m_i} \mathfrak{b}_{i,p}^{F,n-1} - \sum_{p=1}^{m_i} \mathfrak{c}_{i,p}^{F,n-1}, \qquad \text{for } i = 1, \dots, n_F, \\ \mathfrak{a}_i^{T,n-1} &= 1 - \sum_{p=1}^{3} \mathfrak{b}_{i,p}^{T,n-1} - \sum_{p=1}^{3} \mathfrak{c}_{i,p}^{T,n-1}, \qquad \text{for } i = 1, \dots, n_T. \end{aligned}$$

For an appropriately chosen time step τ, we can guarantee the diagonal dominance of the matrix, which means

$$\left|\mathfrak{a}_i^{F,n-1}\right| \geq \sum_{p=1}^{m_i} \left|\mathfrak{b}_{i,p}^{F,n-1}\right| + \sum_{p=1}^{m_i} \left|\mathfrak{c}_{i,p}^{F,n-1}\right|, \qquad \text{for } i = 1, \dots, n_F, \tag{4.40}$$

$$\left|\mathfrak{a}_i^{T,n-1}\right| \geq \sum_{p=1}^{3} \left|\mathfrak{b}_{i,p}^{T,n-1}\right| + \sum_{p=1}^{3} \left|\mathfrak{c}_{i,p}^{T,n-1}\right|, \qquad \text{for } i = 1, \dots, n_T. \tag{4.41}$$

The diagonal dominance is a pleasant property of the matrix, since it enhances convergence of the iterative methods for solving the linear system.

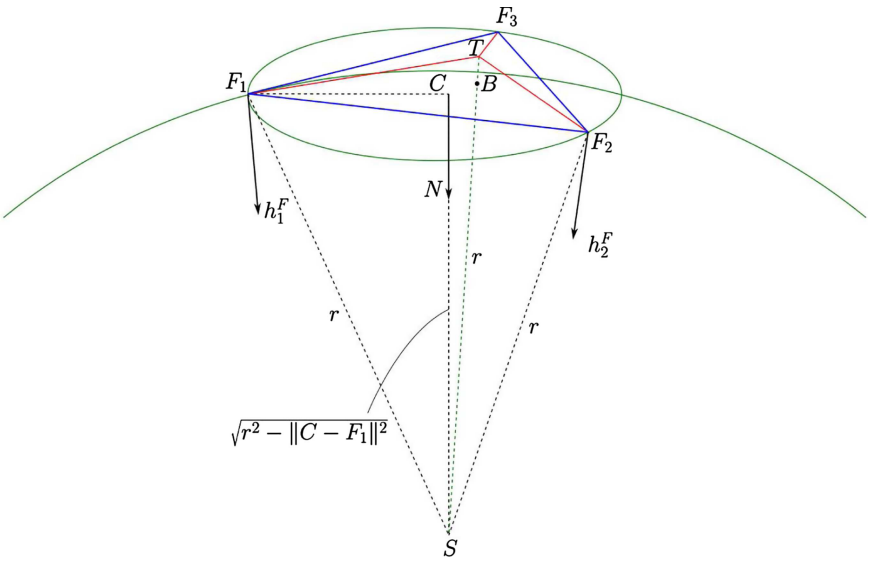

FIGURE 19. Setting the initial position of a T-vertex. The green circle is the circumscribed circle. The green arc is a sketch of the interpolation sphere (Color online).

Implementation note. In our scheme we need the cotangent of the angle ω for each diamond cell V^D. From (4.19) we see that we can compute the cotangent as

$$\cot\omega = \frac{u \cdot v}{\sqrt{\|u\|^2\|v\|^2 - (u \cdot v)^2}}, \tag{4.42}$$

where $u = F_2 - F_1$, $v = T_2 - T_1$ with F_1, T_1, F_2, T_2 being the vertices of the diamond cell V^D.

Initial condition for T-vertices. If we know the initial surface X^0, then we can set both $F_i^0, i = 1, \dots, n_F$ and $T_i^0, i = 1, \dots, n_T$ to lie on the surface X^0. But in a common situation when just the initial triangulation $F_i^0, i = 1, \dots, n_F$ is given, we have to set the initial positions $T_i^0, i = 1, \dots, n_T$. One natural choice is to put a vertex T_i^0 to the barycenter of the corresponding triangle $\mathcal{T}_i^0$. Another reasonable option is to set T_i^0 with respect to the shape of the surface in its neighbourhood.

The basic idea in our implementation is to set the initial position of the vertex T_i according to the mean curvature in neighbouring F-vertices. Such setting can be achieved by the following procedure (Fig. 19).

(1) Place T_i^0 to the barycenter B_i of the triangle with vertices $F_{i,1}^0$, $F_{i,2}^0$, $F_{i,3}^0$ which means

$$T_i^0 = B_i = \tfrac{1}{3}\left(F_{i,1}^0 + F_{i,2}^0 + F_{i,3}^0\right).$$

(2) Calculate the mean curvature vectors $h_{i,p}^F$ in the neighbouring vertices $F_{i,p}^0, p = 1, 2, 3$ using (4.27). Then compute the average mean curvature vector $\langle h_i^F \rangle = \frac{1}{3}\left(h_{i,1}^F + h_{i,2}^F + h_{i,3}^F\right)$.
(3) Find the circumcenter of the triangle by the formula $C_i = (1 - \lambda - \mu)F_{i,1}^0 + \lambda F_{i,2}^0 + \mu F_{i,3}^0$, where

$$\lambda = \frac{(\|u\|^2 - u \cdot v)\|v\|^2}{2(\|u\|^2\|v\|^2 - (u \cdot v)^2)}, \qquad \mu = \frac{(\|v\|^2 - u \cdot v)\|u\|^2}{2(\|u\|^2\|v\|^2 - (u \cdot v)^2)},$$

where $u = F_{i,2}^0 - F_{i,1}^0$ and $v = F_{i,3}^0 - F_{i,1}^0$.

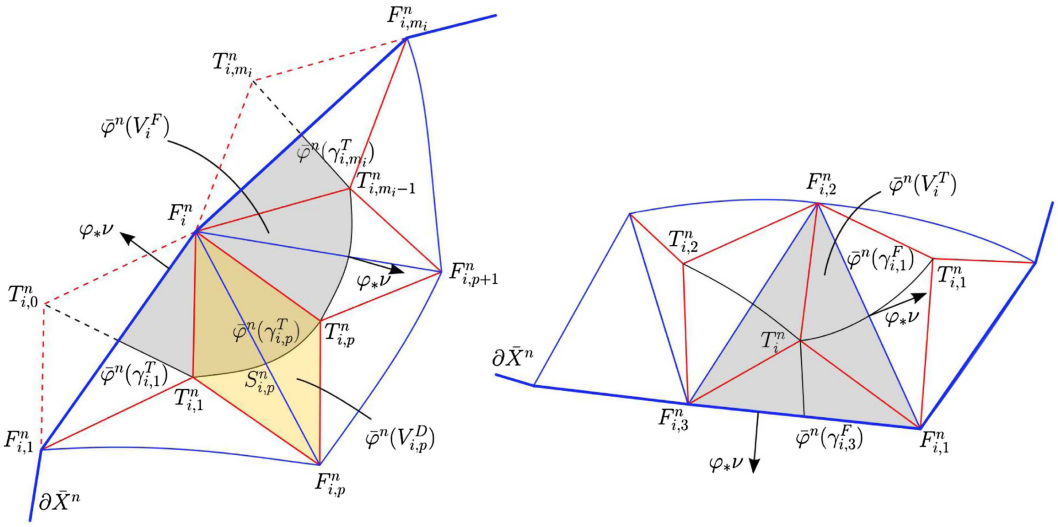

FIGURE 20. *Left panel*: a boundary finite volume V_i^F. *Right panel*: a boundary finite volume V_i^T.

(4) Compute the normal N_i to the triangle as

$$N_i = \frac{u \times v}{\|u \times v\|} \operatorname{sgn}\left((u \times v).\langle h_i^F \rangle\right).$$

The sign function provides the correct orientation of the normal.

(5) Construct the interpolating sphere with the mean curvature equal to $\|\langle h_i^F \rangle\|$. Since the mean curvature of the sphere with radius r is $H = 2/r$ (see Eq. (2.5)), the radius and the center are

$$r_i = \frac{2}{\|\langle h_i^F \rangle\|}, \qquad S_i = C_i + \sqrt{r^2 - \|C_i - F^0_{i,1}\|^2} N_i.$$

(6) Project the barycenter B_i onto the sphere to get the initial position of T-vertex.

$$T_i^0 = S_i + r \frac{B_i - S_i}{\|B_i - S_i\|}.$$

4.2. Discretization of the tangential velocity

In this section we perform a discretization of the tangential velocity for the asymptotically uniform redistribution (2.26). The relative area preserving redistribution (2.25) is easily obtained by setting $\omega = 0$. With appropriate modifications we adopt the technique developed in [27, 43]. To simplify the notation we omit the time index in some equations. All quantities are taken from the $(n-1)$th time step.

4.2.1. System of equations for ψ^F, ψ^T

Let $\psi_i^{F,n} = \psi^n(x_i), i = 1, \dots n_F$ and $\psi_i^{T,n} = \psi^n(b_i), i = 1, \dots n_T$ denote the values of ψ in F- and T-vertices respectively. In this section we derive the system of linear equations for ψ_i^F, ψ_i^T.

Applying the finite volume technique we integrate (2.26) over finite volumes V_i^F and V_i^T. Since we develop a general discretization also for surfaces with boundary, we need to define what are boundary finite volumes. A boundary finite volume V_i^F is such that $F_i^n \in \partial\bar X^n$ (Fig. 20, *left*), and a boundary finite volume V_i^T is such that at least two of the neighbours $F^n_{i,1}, F^n_{i,2}, F^n_{i,3}$ of T_i^n lie on $\partial\bar X^n$ (Fig. 20, *right*).

Integral of Laplace–Beltrami operator. We integrate the formula (2.26) over internal finite volumes and on the left-hand side we have

$$\begin{aligned}\int\limits_{V_i^F} \triangle_{\bar\varphi}\psi \,\mathrm{d}\chi_{\bar\varphi} &\approx \frac{1}{2}\sum_{p=1}^{m_i} q_{i,p}^{FF}(\psi_{i,p}^F-\psi_i^F)+\sum_{p=1}^{m_i}(q_{i,p+1}^{FT}-q_{i,p}^{FT})\psi_{i,p}^T,\\ \int\limits_{V_i^T} \triangle_{\bar\varphi}\psi \,\mathrm{d}\chi_{\bar\varphi} &\approx \frac{1}{2}\sum_{p=1}^{3} q_{i,p}^{TT}(\psi_{i,p}^T-\psi_i^T)+\sum_{p=1}^{3}(q_{i,p-1}^{TF}-q_{i,p}^{TF})\psi_{i,p}^F,\end{aligned} \tag{4.43}$$

with coefficients $q_{i,p}^{FF}, q_{i,p}^{FT}$ and $q_{i,p}^{TT}, q_{i,p}^{TF}$ defined by (4.34) and (4.38) respectively. For a boundary finite volume V_i^F (Fig. 20, *left*) the integration gives

$$\begin{aligned}\int\limits_{V_i^F} \triangle_{\bar\varphi}\psi \mathrm{d}\chi_{\bar\varphi} &= \int\limits_{\partial V_i^F} g_{\bar\varphi}(\nabla_{\bar\varphi}\psi,\nu)\,\mathrm{d}H_\chi = \int\limits_{\partial V_i^F-(\partial V_i^F\cap\partial X)} g_{\bar\varphi}(\nabla_{\bar\varphi}\psi,\nu)\,\mathrm{d}H_\chi = \sum_{p=1}^{m_i}\int\limits_{\gamma_{i,p}^T} g_{\bar\varphi}(\nabla_{\bar\varphi}\psi,\nu)\,\mathrm{d}H_\chi =\\ &\approx \sum_{p=1}^{m_i}\left[\frac{1}{2}q_{i,p}^{FF}(\psi_{i,p}^F-\psi_i^F)-q_{i,p}^{FT}(\psi_{i,p}^T-\psi_{i,p-1}^T)\right],\end{aligned}$$

where the integral over $\partial V_i\cap\partial X$ vanished due to Neumann boundary condition (2.29). Now we substitute $\psi_{i,0}^T=\psi_i^F+\psi_{i,1}^F-\psi_{i,1}^T$ and $\psi_{i,m_i}^T=\psi_i^F+\psi_{i,1}^F-\psi_{i,1}^T$ (see Eq. (4.3) and also Fig. 20, *left*) and obtain

$$\begin{aligned}\int\limits_{V_i^F} \triangle_{\bar\varphi}\psi \mathrm{d}\chi_{\bar\varphi} \approx{}& \left[-\frac{1}{2}\sum_{p=1}^{m_i} q_{i,p}^{FF}+(q_{i,1}^{FT}-q_{i,m_i}^{FT})\right]\psi_i^F\\ &+\left[\frac{1}{2}q_{i,1}^{FF}+q_{i,1}^{FT}\right]\psi_{i,1}^F+\frac{1}{2}\sum_{p=2}^{m_i-1}q_{i,p}^{FF}\psi_{i,p}^F+\left[\frac{1}{2}q_{i,m_i}^{FF}-q_{i,m_i}^{FT}\right]\psi_{i,m_i}^F\\ &+\left[-2q_{i,1}^{FT}+q_{i,2}^{FT}\right]\psi_{i,1}^T+\sum_{p=2}^{m_i-2}\left(-q_{i,p}^{FT}+q_{i,p+1}^{FT}\right)\psi_{i,p}^T+\left[-q_{i,m_i-1}^{FT}+2q_{i,m_i}^{FT}\right]\psi_{i,m_i-1}^T.\end{aligned} \tag{4.44}$$

For a boundary finite volume V_i^T (Fig. 20, *right*) the integration follows

$$\begin{aligned}\int\limits_{V_i^T} \triangle_{\bar\varphi}\psi \mathrm{d}\chi_{\bar\varphi} &= \sum_{p=1}^{2}\int\limits_{\gamma_{i,p}^F} g_{\bar\varphi}(\nabla_{\bar\varphi}\psi,\nu)\,\mathrm{d}H_\chi\\ &\approx \sum_{p=1}^{3}\left[\frac{1}{2}q_{i,p}^{TT}(\psi_{i,p}^T-\psi_i^T)-q_{i,p}^{TF}(\psi_{i,p}^F-\psi_{i,p+1}^F)\right]\\ &= -\frac{1}{2}\left(q_{i,1}^{TT}+q_{i,2}^{TT}\right)\psi_i^T+\frac{1}{2}q_{i,1}^{TT}\psi_{i,1}^T+\frac{1}{2}q_{i,2}^{TT}\psi_{i,2}^T\\ &\quad -q_{i,1}^{TF}\psi_{i,1}^F+\left(q_{i,1}^{TF}-q_{i,2}^{TF}\right)\psi_{i,2}^F+q_{i,2}^{TF}\psi_{i,3}^F.\end{aligned} \tag{4.45}$$

The integral over $\gamma_{i,3}^F$ vanished due to Neumann boundary condition (2.29).

Integral of the right-hand side. Since the boundary of the surface is static, we have $v_N = 0$ for boundary vertices. We can use the following approximation of the first term on the right-hand side in (2.26)

$$\begin{aligned}\int_{V_i^F} g_Y(v_N,h)\mathrm{d}\chi_{\bar\varphi} &\approx A_i^F g_Y(v_{N,i},h_i^F) = \begin{cases} A_i^F (H_i^F)^2 & \text{if } F_i^n \notin \partial\bar X^n \\ 0 & \text{if } F_i^n \in \partial\bar X^n \end{cases},\\ \int_{V_i^T} g_Y(v_N,h)\mathrm{d}\chi_{\bar\varphi} &\approx A_i^T g_Y(v_{N,i},h_i^T) = A_i^T (H_i^T)^2,\end{aligned} \tag{4.46}$$

and for the second term we have

$$\begin{aligned}\int_{V_i^F} \langle g_Y(v_N,h)\rangle_{\chi_{\bar\varphi}}\mathrm{d}\chi_{\bar\varphi} &\approx A_i^F \langle g_Y(v_N,h)\rangle_{\chi_{\bar\varphi}} \approx \frac{A_i^F}{A}\sum_{j,F_j\notin\partial\bar X}(H_j^F)^2 A_j^F,\\ \int_{V_i^T} \langle g_Y(v_N,h)\rangle_{\chi_{\bar\varphi}}\mathrm{d}\chi_{\bar\varphi} &\approx A_i^T \langle g_Y(v_N,h)\rangle_{\chi_{\bar\varphi}} \approx \frac{A_i^T}{A}\sum_{j=1}^{n_T}(H_j^T)^2 A_j^T.\end{aligned} \tag{4.47}$$

For a proper approximation of the last term we introduce the angular size μ_i of a finite volume V_i^F and a reduced number of F-vertices n_F^* as follows

$$\mu_i = \frac{\alpha_i}{2\pi}, \qquad n_F^* = \sum_{i=1}^{n_F}\mu_i. \tag{4.48}$$

For an internal F-we define $\alpha_i = 2\pi$, resulting in $\mu_i = 1$, and, for a boundary vertex, α_i is the angle between vectors $\overrightarrow{F_iF_{i,1}}$ and $\overrightarrow{F_iF_{i,m_i}}$, see Figure 20. Now we need to approximate the area density G_i^F. Since the total surface area A can be computed in two ways

$$\begin{aligned}A &= \int_X \mathrm{d}\chi_{\bar\varphi^{n-1}} = \sum_{i=1}^{n_F}\chi_{\bar\varphi^{n-1}}(V_i^F),\\ A &= \int_X G(x,t^{n-1})\mathrm{d}\xi \approx \sum_{i=1}^{n_F} G_i^F \xi(V_i^F),\end{aligned} \tag{4.49}$$

we have $G_i^F = \frac{\chi_{\bar\varphi^{n-1}}(V_i^F)}{\xi(V_i^F)} = \frac{A_i^F}{\xi(V_i^F)}$ and analogously $G_i^T = \frac{A_i^T}{\xi(V_i^T)}$. We do not have any conditions imposed on the measure ξ. For the asymptotically uniform redistribution it is reasonable to set

$$\xi(V_i^F) = \mu_i\frac{\xi(X)}{n_F^*} = \frac{\mu_i}{Cn_F^*}, \qquad \xi(V_i^T) = \frac{\xi(X)}{n_T} = \frac{1}{Cn_T},$$

where we used that $\xi(X) = \frac{1}{C}$ holds (see the discussion below (2.21)). The approximation of the area density follows

$$G_i^F = \frac{Cn_F^* A_i^F}{\mu_i}, \qquad G_i^T = Cn_T A_i^T.$$

Finally, the approximations of the integrals over the last term on the right-hand side of (2.26) are given by

$$\begin{aligned}\int_{V_i^F}\left(C\frac{A}{G}-1\right)\omega\mathrm{d}\chi_{\bar\varphi} &\approx A_i^F\left(\frac{A\mu_i}{n_F^* A_i^F}-1\right)\omega,\\ \int_{V_i^T}\left(C\frac{A}{G}-1\right)\omega\mathrm{d}\chi_{\bar\varphi} &\approx A_i^T\left(\frac{A}{n_T A_i^T}-1\right)\omega.\end{aligned} \tag{4.50}$$

Final equations. Now we put the approximations (4.43)–(4.50) together to obtain the system of equations for $\psi_i^{F,n-1}, \psi_i^{T,n-1}$. In following, the coefficients $q_{i,p}^{FF}, q_{i,p}^{FT}$ and $q_{i,p}^{TT}, q_{i,p}^{TF}$ are defined by (4.34) and (4.38) respectively.

Internal covolumes V_i^F

$$\hat{\mathfrak{a}}_i^F \psi_i^F + \sum_{p=1}^{m_i} \hat{\mathfrak{b}}_{i,p}^F \psi_{i,p}^F + \sum_{p=1}^{m_i} \hat{\mathfrak{c}}_{i,p}^F \psi_{i,p}^T = (H_i^F)^2 - \frac{1}{A} \sum_{j, F_j \notin \partial \bar{X}} (H_j^F)^2 A_j^F + \left(\frac{A}{n_F^* A_i^F} - 1 \right) \omega \tag{4.51}$$

for i such that F_i is an internal vertex and where

$$\hat{\mathfrak{a}}_i^F = -\frac{1}{2A_i^F} \sum_{p=1}^{m_i} q_{i,p}^{FF}, \qquad \hat{\mathfrak{b}}_{i,p}^F = \frac{1}{2A_i^F} q_{i,p}^{FF}, \qquad \hat{\mathfrak{c}}_{i,p}^F = \frac{1}{A_i^F} \left(-q_{i,p}^{FT} + q_{i,p+1}^{FT} \right) \tag{4.52}$$

for $p = 1, \ldots, m_i$.

Boundary covolumes V_i^F

$$\hat{\mathfrak{a}}_i^F \psi_i^F + \sum_{p=1}^{m_i} \hat{\mathfrak{b}}_{i,p}^F \psi_{i,p}^F + \sum_{p=1}^{m_i - 1} \hat{\mathfrak{c}}_{i,p}^F \psi_{i,p}^T = -\frac{1}{A} \sum_{j, F_j \notin \partial \bar{X}} H_j^2 A_j^F + \left(\frac{A \mu_i}{n_F^* A_i} - 1 \right) \omega \tag{4.53}$$

for i such that F_i is a boundary vertex and where

$$\begin{aligned}
\hat{\mathfrak{a}}_i^F &= \frac{1}{2A_i^F} \left[-\sum_{p=1}^{m_i} q_{i,p}^{FF} + 2(q_{i,1}^{FT} - q_{i,m_i}^{FT}) \right] \\
\hat{\mathfrak{b}}_{i,1}^F &= \frac{1}{2A_i^F} \left(q_{i,1}^{FF} + 2q_{i,1}^{FT} \right), \qquad \hat{\mathfrak{b}}_{i,m_i}^F = \frac{1}{2A_i^F} \left(q_{i,m_i}^{FF} - 2q_{i,m_i}^{FT} \right), \\
\hat{\mathfrak{b}}_{i,p}^F &= \frac{1}{2A_i^F} q_{i,p}^{FF}, \qquad p = 2, \ldots, m_i - 1, \\
\hat{\mathfrak{c}}_{i,1}^F &= \frac{1}{A_i^F} \left(-2q_{i,1}^{FT} + q_{i,2}^{FT} \right), \qquad \hat{\mathfrak{c}}_{i,m_i-1}^F = \frac{1}{A_i^F} \left(-q_{i,m_i-1}^{FT} + 2q_{i,m_i}^{FT} \right), \\
\hat{\mathfrak{c}}_{i,p}^F &= \frac{1}{A_i^F} \left(-q_{i,p}^{FT} + q_{i,p+1}^{FT} \right), \qquad p = 2, \ldots, m_i - 2.
\end{aligned} \tag{4.54}$$

Internal covolumes V_i^T

$$\hat{\mathfrak{a}}_i^T \psi_i^T + \sum_{p=1}^{3} \hat{\mathfrak{b}}_{i,p}^T \psi_{i,p}^T + \sum_{p=1}^{3} \hat{\mathfrak{c}}_{i,p}^T \psi_{i,p}^F = (H_i^T)^2 - \frac{1}{A} \sum_{j=1}^{n_T} (H_j^T)^2 A_j^T + \left(\frac{A}{n_T A_i^T} - 1 \right) \omega \tag{4.55}$$

for i such that V_i^T is an internal finite volume and where

$$\hat{\mathfrak{a}}_i^T = -\frac{1}{2A_i^T} \sum_{p=1}^{3} q_{i,p}^{TT}, \qquad \hat{\mathfrak{b}}_{i,p}^T = \frac{1}{2A_i^T} q_{i,p}^{TT}, \qquad \hat{\mathfrak{c}}_{i,p}^T = \frac{1}{A_i^T} \left(q_{i,p-1}^{TF} - q_{i,p}^{TF} \right) \tag{4.56}$$

for $p = 1, 2, 3$.

Boundary covolumes V_i^T

The equation (4.55) is valid, but the second sum runs only over $p = 1, 2$, and the coefficients (4.56) modify to

$$\begin{aligned}
\hat{\mathfrak{a}}_i^T &= -\frac{1}{2A_i^T} \left(q_{i,1}^{TT} + q_{i,2}^{TT} \right), \qquad \hat{\mathfrak{b}}_{i,p}^T = \frac{1}{2A_i^T} q_{i,1}^{TT}, \quad p = 1, 2 \\
\hat{\mathfrak{c}}_{i,1}^T &= -\frac{1}{A_i^T} q_{i,1}^{TF}, \qquad \hat{\mathfrak{c}}_{i,2}^T = \frac{1}{A_i^T} \left(q_{i,1}^{TF} - q_{i,2}^{TF} \right), \qquad \hat{\mathfrak{c}}_{i,3}^T = \frac{1}{A_i^T} q_{i,2}^{TF}.
\end{aligned} \tag{4.57}$$

For closed surfaces there are no boundary covolumes ($\mu_i = 1, i = 1, \dots, n_F$ and $n_F^* = n_F$) and the equation (4.51) modifies to

$$\hat{\mathfrak{a}}_i^F \psi_i^F + \sum_{p=1}^{m_i} \hat{\mathfrak{b}}_{i,p}^F \psi_{i,p}^F + \sum_{p=1}^{m_i} \hat{\mathfrak{c}}_{i,p}^F \psi_{i,p}^T = (H_i^F)^2 - \frac{1}{A} \sum_{j=1}^{n_F} (H_j^F)^2 A_j^F + \left(\frac{A}{n_F A_i^F} - 1 \right) \omega \tag{4.58}$$

for $i = 1, \dots, n_F$. For closed surfaces the equation (4.55) holds for all $i = 1, \dots, n_T$.

Uniqueness of the solution. The linear system of equations for unknowns ψ_i^F, $i = 1, \dots, n_F$ and ψ_i^T, $i = 1, \dots, n_T$ can be represented by a $n_V \times n_V$ matrix, $n_V = n_F + n_T$. The kernel of the matrix contains a n_V-dimensional vector

$$(\underbrace{c_1, \dots, c_1}_{n_F}, \underbrace{c_2, \dots, c_2}_{n_T}), \qquad c_1, c_2 \in \mathbb{R}, \tag{4.59}$$

which means the solution of the system is not unique. The equations for $V_1^F, \dots, V_{n_F}^F$ are not linearly independent, and the same is true for the equations for $V_1^T, \dots, V_{n_T}^T$.

It would not be correct to apply (2.27) and fix the solution in one specific ψ_i^F and one ψ_j^T, *e.g.* $\psi_i^F = 2$ and $\psi_j^T = 5$, since we do not know anything about the relationship between the values ψ_i^F and ψ_j^F.

Instead we will use (2.28) to fix the mean value of ψ over X. The mean value can be computed in two ways

$$\langle \psi \rangle_{\chi_{\bar\varphi}} = \frac{1}{A} \int_X \psi(x) \mathrm{d}\chi_{\bar\varphi} \overset{1.}{\approx} \frac{1}{A} \sum_{i=1}^{n_F} \psi_i^F A_i^F, \qquad \overset{2.}{\approx} \frac{1}{A} \sum_{i=1}^{n_T} \psi_i^T A_i^T.$$

We fix the mean value to $\langle \psi \rangle_{\chi_{\bar\varphi}} = 0$, which means

$$\sum_{i=1}^{n_F} \psi_i^F A_i^F = 0, \qquad \sum_{i=1}^{n_T} \psi_i^T A_i^T = 0. \tag{4.60}$$

In practice we modify the system of linear equations by replacing the equations for V_1^F and V_1^T by (4.60).

Note that there is no possibility to guarantee the diagonal dominance (4.40) of the matrix of the linear system for ψ_i^F, $i = 1, \dots, n_F$ and ψ_i^T, $i = 1, \dots, n_T$. Therefore, for the iterative methods, the system for ψ_i^F, ψ_i^T is much more difficult to solve than the system for F_i^n and T_i^n.

4.2.2. Calculation of tangential velocity from ψ^F, ψ^T

To calculate the tangential velocities

$$v_{T,i}^F \approx \frac{1}{A_i^F} \int_{V_i} v_T \mathrm{d}\chi_{\bar\varphi}, \qquad v_{T,i}^T \approx \frac{1}{A_i^T} \int_{V_i} v_T \mathrm{d}\chi_{\bar\varphi}$$

from ψ_i^F, ψ_i^T we use the following identity (see [14])

$$\int_{V_i} v_T^{n-1} \mathrm{d}\chi_{\bar\varphi^{n-1}} = \bar\varphi_*^{n-1} \left(\int_{\partial V_i} \psi^{n-1} \nu_i^{n-1} \mathrm{d}H_{\chi_{\bar\varphi^{n-1}}} \right) - \int_{V_i} \psi^{n-1} h^{n-1} \mathrm{d}\chi_{\bar\varphi^{n-1}}, \tag{4.61}$$

which can be approximated as follows

$$\int_{V_i^F} v_T \mathrm{d}\chi_{\bar\varphi} \approx \sum_{p=1}^{m_i} |\gamma_{i,p}^T| \psi_{i,p}^D (\bar\varphi_* \nu_{i,p}^F) - \psi_i^F h_i^F A_i^F, \tag{4.62}$$

$$\int_{V_i^T} v_T \mathrm{d}\chi_{\bar\varphi} \approx \sum_{p=1}^{3} |\gamma_{i,p}^F| \psi_{i,p}^D (\bar\varphi_* \nu_{i,p}^T) - \psi_i^T h_i^T A_i^T, \tag{4.63}$$

where the normals $\bar{\varphi}_* \nu^F_{i,p}$ and $\bar{\varphi}_* \nu^T_{i,p}$ are calculated by (4.20) and (4.24) respectively. The symbol $\psi^D_{i,p}$ denotes the value of ψ in the middle of the neighbouring diamond cell $V^D_{i,p}$. For an internal diamond cell V^D with vertices F_1, F_2, T_1, T_2 we compute the value ψ^D as

$$\psi^D = \frac{1}{4}\left(\psi^F_1 + \psi^F_2 + \psi^T_1 + \psi^T_2\right), \tag{4.64}$$

and in case of a boundary diamond cell $\psi^D = \frac{1}{2}\left(\psi^F_1 + \psi^F_2\right)$.

5. Numerical experiments

In this section we test the numerical scheme in several numerical experiments. We perform experiments with both closed surfaces and surfaces with boundary, and compare the evolution with no redistribution to evolution with area-oriented redistribution. As in Section 3, we use the BiCGStab (BiConjugate Gradient Stabilized) method (see [45]) to solve systems of linear equations for both position vectors $F^n_i, i = 1, \ldots, n_F$; $T^n_i, i = 1, \ldots, n_T$ and velocity potential $\psi^{F,n-1}_i, i = 1, \ldots, n_F$; $\psi^{T,n-1}_i, i = 1, \ldots, n_T$.

5.1. Closed surfaces

First we test the performance of the method on closed surfaces. If the initial condition X^0 is a unit sphere, then the surface X^t evolving by mean curvature flow (2.7) is a shrinking sphere with radius

$$r(t) = \sqrt{1 - 4t}. \tag{5.1}$$

The knowledge of the exact solution allows us to calculate the time-space L^2 error as follows (taking into account both errors of F- and T-vertices)

$$L^2 \text{ error} = \left[\sum_{n=1}^{N}\left(\sum_{i=1}^{n_F}\left(\|F^n_i\| - r(t^n)\right)^2 \frac{A^F_i}{2} + \sum_{i=1}^{n_T}\left(\|T^n_i\| - r(t^n)\right)^2 \frac{A^T_i}{2}\right)\tau\right]^{\frac{1}{2}}. \tag{5.2}$$

We also study the experimental order of convergence (EOC) of the method calculated as follows

$$\text{EOC} = \log_2\left(\frac{L^2 \text{ error}_h}{L^2 \text{ error}_{h/2}}\right), \tag{5.3}$$

where L^2 error$_h$ is the L^2 error for a mesh with characteristic edge length h.

We use a discretization of the sphere based on the division of the regular icosahedron. The diamond mesh (see Fig. 21) was created by modifying a triangular mesh as we described in Section 4.1.1. The initial positions of T-vertices were set using the procedure described before in Section 4.2.

The final time was set to $t_f = 0.08$. We adopt a standard coupling for parabolic problems $\tau \sim h^2$ (with h denoting a characteristic edge length).

The method was tested both with no tangential redistribution and with asymptotically uniform redistribution with $\omega = 1, 10$ and 100. The results are presented in Tables 1–4. In the tables, "FT-iter" and "ψ-iter" are the total numbers (summed over all time steps) of iterations of the BiCGStab method needed to solve the systems for position vectors $F^n_i, i = 1, \ldots, n_F$; $T^n_i, i = 1, \ldots, n_T$ and velocity potential $\psi^{F,n-1}_i, i = 1, \ldots, n_F$; $\psi^{T,n-1}_i, i = 1, \ldots, n_T$, respectively. The average values per time step are denoted by $\langle FT\text{-iter}\rangle$ and $\langle\psi\text{-iter}\rangle$. The experimental order of convergence (EOC) is computed by the formula (5.3). Similarly as in cotangent scheme, we observe higher computational demands (number of iterations of BiCGStab) for solving the system for ψ compared to solving the system for position vectors. This is due to the properties of the system matrices, see the note at the end of the Sect. 4.2.1).

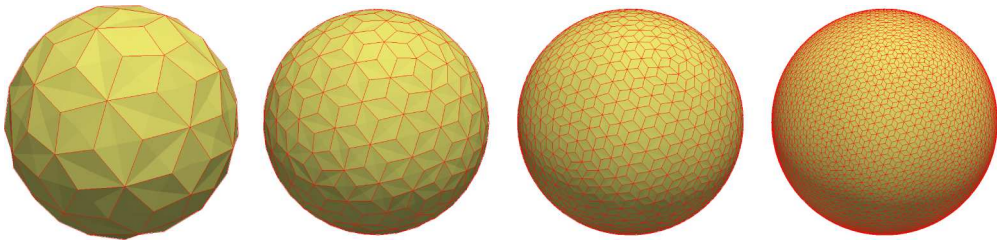

FIGURE 21. The discretization of the unit sphere with diamond mesh displayed, from left to right: $n_V = 122, 482, 1922, 7682$.

TABLE 1. The L^2 EOC for the case with no redistribution.

n_V	n_F	n_T	τ	N	L^2 error	FT-iter	$\langle FT\text{-iter}\rangle$	EOC
122	42	80	0.04	2	1.43e-02	8	4.00	
482	162	320	0.01	8	3.35e-03	37	4.63	2.10
1922	642	1280	0.0025	32	8.07e-04	146	4.56	2.05
7682	2562	5120	0.000625	128	1.95e-04	419	3.27	2.05
30 722	10 242	20 480	0.00015625	512	4.64e-05	1216	2.38	2.07

TABLE 2. The L^2 EOC for the case with asymptotically uniform redistribution, $\omega = 1$.

n_V	τ	N	L^2 error	FT-iter	$\langle FT\text{-iter}\rangle$	ψ-iter	$\langle\psi\text{-iter}\rangle$	EOC
122	0.04	2	3.40e-02	9	4.50	78	39.00	
482	0.01	8	9.08e-03	40	5.00	704	88.00	1.90
1922	0.0025	32	2.30e-03	147	4.59	6408	200.25	1.98
7682	0.000625	128	5.78e-04	512	4.00	37 199	290.62	2.00
30 722	0.00015625	512	1.44e-04	1745	3.41	241 137	470.97	2.00

TABLE 3. The L^2 EOC for the case with asymptotically uniform redistribution, $\omega = 10$.

n_V	τ	N	L^2 error	FT-iter	$\langle FT\text{-iter}\rangle$	ψ-iter	$\langle\psi\text{-iter}\rangle$	EOC
122	0.04	2	3.41e-02	9	4.50	94	47.00	
482	0.01	8	9.10e-03	42	5.25	736	92.00	1.91
1922	0.0025	32	2.31e-03	162	5.06	6897	215.53	1.98
7682	0.000625	128	5.78e-04	604	4.72	47 494	371.05	2.00
30 722	0.00015625	512	1.45e-04	2048	4.00	41 9643	819.62	2.00

TABLE 4. The L^2 EOC for the case with asymptotically uniform redistribution, $\omega = 100$.

n_V	τ	N	L^2 error	FT-iter	$\langle FT\text{-iter}\rangle$	ψ-iter	$\langle\psi\text{-iter}\rangle$	EOC
122	0.04	2	3.77e-02	9	4.50	72	36.00	
482	0.01	8	9.24e-03	47	5.88	774	96.75	2.03
1922	0.0025	32	2.33e-03	168	5.25	6407	200.22	1.99
7682	0.000625	128	5.84e-04	593	4.63	51 861	405.16	2.00
30 722	0.00015625	512	1.46e-04	2095	4.09	468 117	914.29	2.00

TABLE 5. The H^1 error and EOC for the case with no redistribution compared with cotangent scheme.

n_V	n_F	n_T	τ	N	H^1_{DDFV} error	EOC	H^1_{COT} error	EOC
122	42	80	0.04	2	1.57e-02		3.09e-02	
482	162	320	0.01	8	3.34e-03	2.23	1.61e-02	0.94
1922	642	1280	0.0025	32	1.23e-03	1.44	8.65e-03	0.90
7682	2562	5120	0.000625	128	4.94e-04	1.32	4.44e-03	0.96
30 722	10 242	20 480	0.00015625	512	1.92e-04	1.36	2.24e-03	0.99

TABLE 6. The error and EOC of the surface normals for the case with no redistribution compared with cotangent scheme.

n_V	n_F	n_T	τ	N	N_{DDFV} error	EOC	N_{COT} error	EOC
122	42	80	0.04	2	1.11E-02		2.19e-02	
482	162	320	0.01	8	2.36E-03	2.23	1.14e-02	0.94
1922	642	1280	0.0025	32	8.71E-04	1.44	6.12e-03	0.90
7682	2562	5120	0.000625	128	3.50E-04	1.32	3.14e-03	0.96
30 722	10 242	20 480	0.00015625	512	1.36E-04	1.36	1.58e-03	0.99

Looking at the tables, we see that the experimental order of convergence of DDFV method is equal to 2 in all presented cases when using the coupling $\tau \sim h^2$. Comparing the L^2 errors we see that the tangential redistribution introduces an extra error. The L^2 error increases with increasing ω, which is a behaviour present also in cotangent scheme). However, the method still converges with no loss of the convergence rate in all cases. For the case with no redistribution we compute also the time-space H^1 (energy) error defined as

$$H^1 \text{ error} = \left[\int_0^{t_f} \left(\int_X \sum_{i,j=1}^{3} g\left(\nabla_g \varepsilon^i, \nabla_g \varepsilon^j\right) \mathrm{d}\chi_\varphi \right) \mathrm{d}t \right]^{\frac{1}{2}}, \tag{5.4}$$

where we denoted $\varepsilon = \bar{\varphi} - \varphi$. After discretization we obtain quite complicated formula

$$H^1_{\mathrm{DDFV}} \text{ error} = \left[\sum_{n=1}^{N} \left(\sum_{i=1}^{n_{\mathrm{dia}}} \left(4 - \frac{2\left(\|U\|^2 \|V \times N(S)\|^2 - 2(U \cdot V)(U \times N(S))(V \times N(S)) + \|V\|^2 \|U \times N(S)\|^2 \right)}{\|U\|^2 \|V\|^2 - (U \cdot V)^2} \right) \hat{A}_i^D \right) \tau \right]^{\frac{1}{2}},$$

where $U = \frac{1}{2}(u - v)$, $V = \frac{1}{2}(u + v)$ with u, v defined in (4.8) and $N(S) = N(S_i^n, t^n)$ being the exact surface normal in the center S_i^n of the diamond cell $V_i^{D,n}$ and $\hat{A}_i^D$ denotes the area of the diamond cell. Additionally, we study the time-space error of surface normals. which is also a quantity related to first derivative of the solution (similarly as gradient in H^1 norm). We use following formula

$$N_{\mathrm{DDFV}} \text{ error} = \left[\sum_{n=1}^{N} \left(\sum_{i=1}^{n_{\mathrm{dia}}} \|N_i^{D,n} - N(S_i^n, t^n)\|^2 \hat{A}_i^D \right) \tau \right]^{\frac{1}{2}}, \tag{5.5}$$

where $N_i^{D,n}$ denotes the surface normal in the center S_i^n of the diamond cell $V_i^{D,n}$. We compare these errors to the cotangent scheme in Tables 5 and 6 respectively.

In the calculation of errors we evaluate the gradients and normals on the diamond cells in the case of DDFV method, and on the mesh triangles in the cotangent scheme, since these are the basic discretization objects for the schemes. For the cotangent scheme we used meshes with n_F vertices and n_T triangles, while the initial triangulation was constructed using the initial condition $F_i^0, i = 1, \dots, n_F$ from DDFV method. The H^1_{COT} and N_{COT} errors are computed as follows

$$H^1_{\mathrm{COT}} \text{ error} = \left[\sum_{n=1}^{N}\left(\sum_{i=1}^{n_T}\left(4 - \frac{2\left(\|u\|^2\|v\times N(T)\|^2 - 2(u\cdot v)(u\times N(T))(v\times N(T)) + \|v\|^2\|u\times N(T)\|^2\right)}{\|u\|^2\|v\|^2 - (u\cdot v)^2}\right)A_i^T\right)\tau\right]^{\frac{1}{2}},$$

$$N_{\mathrm{COT}} \text{ error} = \left[\sum_{n=1}^{N}\left(\sum_{i=1}^{n_T}\|N_i^{T,n} - N(T_i^n, t^n)\|^2 A_i^T\right)\tau\right]^{\frac{1}{2}},$$

where $N_i^{T,n}$ denotes the surface normal to the triangle $\mathcal{T}_i^n$, $N(T) = N(T_i^n, t^n)$ is the corresponding exact surface normal at barycenter T_i^n, A_i^T denotes the triangle area and $u = F_{i,p}^n - F_i^n$, $v = F_{i,p+1}^n - F_i^n$. In Table 5 we observe that DDFV method gives higher EOC in H^1 norm and Table 6 shows also higher EOC in the computation of surface normals compared to the cotangent scheme.

The second example is the mean curvature flow of a bumpy sphere with the initial condition X^0 (see Fig. 22) parametrized as

$$\begin{aligned} x(\theta,\phi) &= (1 + 0.25\cos 5\theta\,\sin 5\phi)\cos\theta\,\cos\phi,\\ y(\theta,\phi) &= (1 + 0.25\cos 5\theta\,\sin 5\phi)\cos\theta\,\sin\phi,\\ z(\theta,\phi) &= 1.15\sin\theta, \end{aligned}$$

where $\theta \in [-\pi/2, \pi/2]$ and $\phi \in [0, 2\pi]$.

The parameters were set to $t_f = 0.08$, $\tau = 0.000625$. We performed both experiment with no tangential redistribution and with asymptotically uniform tangential redistribution with $\omega = 100$, see Figure 23. In the case with no redistribution we observe a contraction of the mesh (smaller areas of finite volumes) in the regions with relatively high initial curvature (on the hills and in the holes of the bumpy sphere). The right column of Figure 23 shows that the tangential redistribution prevents the mesh contraction.

To study the evolution of the uniformity of the mesh we introduce the relative standard deviation (RSD) of the covolume areas

$$\mathrm{RSD}^{F,n} = \sqrt{\frac{1}{n_F^*}\sum_{i=1}^{n_F}\left(\frac{A_i^{F,n} n_F^*}{A^n} - \mu_i\right)^2}, \qquad \mathrm{RSD}^{T,n} = \sqrt{\frac{1}{n_T}\sum_{i=1}^{n_T}\left(\frac{A_i^{T,n} n_T}{A^n} - 1\right)^2}, \tag{5.6}$$

with $\mathrm{RSD}^{F,n}$ and $\mathrm{RSD}^{T,n}$ measuring the uniformity of the areas of covolumes corresponding to F- and T-vertices, respectively. If the mesh is uniform, *i.e.* $A_i^{F,n} = \frac{A^n}{n_F^*}\mu_i$ and $A_i^{T,n} = \frac{A^n}{n_T}$, then both $\mathrm{RSD}^{F,n} = 0$ and $\mathrm{RSD}^{T,n} = 0$. The relative standard deviations $\mathrm{RSD}^{F,n}$ and $\mathrm{RSD}^{T,n}$ grow with increasing nonuniformity.

The last example in this section is a volume preserving mean curvature flow of a cymling-like shape with $n_V = 7682$, $n_F = 2562$ and $n_T = 5120$ (Fig. 24, top). The volume preserving mean curvature flow is a variation of MCF given by $\partial_t\varphi = \triangle_{g_\varphi}\varphi - \bar{h}$, where $\bar{h} = \bar{H}N$ and $\bar{H}$ is the average mean curvature over X, which is calculated as $\bar{H} = \frac{1}{A}\int_X H \mathrm{d}\chi_\varphi$. Addition of the term $-\bar{h}$ to the standard mean curvature flow ensures preservation of the volume enclosed by the surface. The right-hand side of (4.32) changes to $F_i^{n-1} - \tau\bar{H}_i^{F,n-1}N_i^{F,n-1} + \tau v_{T,i}^{F,n-1}$ and the formula (4.36) changes analogously. The right-hand side of equation (4.58) modifies to

$$\left(\left(H_i^F\right)^2 - \bar{h}_i^F\cdot h_i^F\right) - \frac{1}{A}\sum_{j=1}^{n_F}\left(\left(H_j^F\right)^2 - \bar{h}_j^F\cdot h_j^F\right)A_j^F + \left(\frac{A}{n_F A_i^F} - 1\right)\omega \tag{5.7}$$

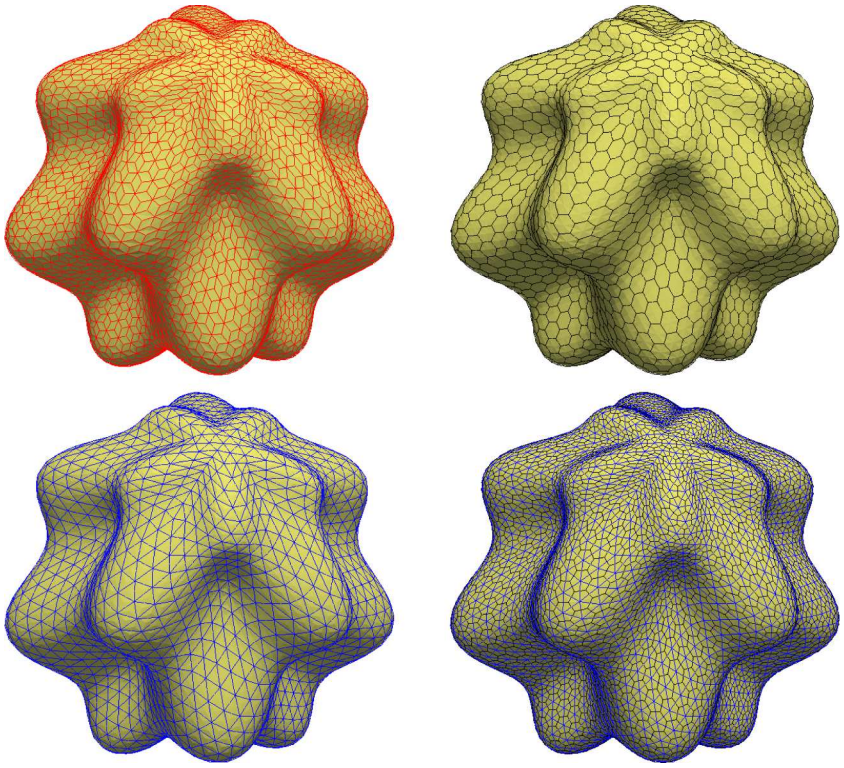

FIGURE 22. A discretization of the bumpy sphere with $n_V = 7682$, $n_F = 2562$ and $n_T = 5120$. Edges of various meshes are displayed. From the top left, diamond mesh, F-covolumes mesh, T-covolumes mesh, both F- and T-covolumes meshes.

and analogously for T-vertices. The initial condition X^0 is parametrized as

$$\begin{aligned} x(\theta,\phi) &= \left(0.15\cos 4\theta + \frac{0.5\sin 8\phi}{\sqrt{2\pi}} e^{-50\,\theta^2} + 0.85\right)\cos\theta\,\cos\phi, \\ y(\theta,\phi) &= \left(0.15\cos 4\theta + \frac{0.5\sin 8\phi}{\sqrt{2\pi}} e^{-50\,\theta^2} + 0.85\right)\cos\theta\,\sin\phi, \\ z(\theta,\phi) &= 0.5\left(0.15\cos 4\theta + \frac{0.5\sin 8\phi}{\sqrt{2\pi}} e^{-50\,\theta^2} + 0.85\right)\sin\theta, \end{aligned} \tag{5.8}$$

where $\theta \in [-\pi/2, \pi/2]$ and $\phi \in [0, 2\pi]$. The final time and time step were set to $t_f = 0.1875$ and $\tau = 0.000625$ respectively.

We did experiments with no redistribution and with asymptotically uniform redistribution with $\omega = 0, 1, 10$ and 100. The evolving surfaces are plotted in Figure 24. As in the experiment above, with no redistribution included we observe a mesh contraction in highly curved regions. However, in this experiment the contraction is much more devastating. Figure 25, left shows the contraction of the mesh in detail. The computation did not crash yet but leads to obviously wrong results. In case of the evolution with asymptotically uniform redistribution we obtain substantially better results. The evolution of RSD of the covolume areas is plotted in Figure 26. In the case with no redistribution RSD grows due to shrinking covolumes. The case $\omega = 0$ corresponds to the relative area preserving redistribution, therefore RSD remains approximately constant. For $\omega = 1, 10, 100$ we observe faster uniformisation of the mesh with higher ω.

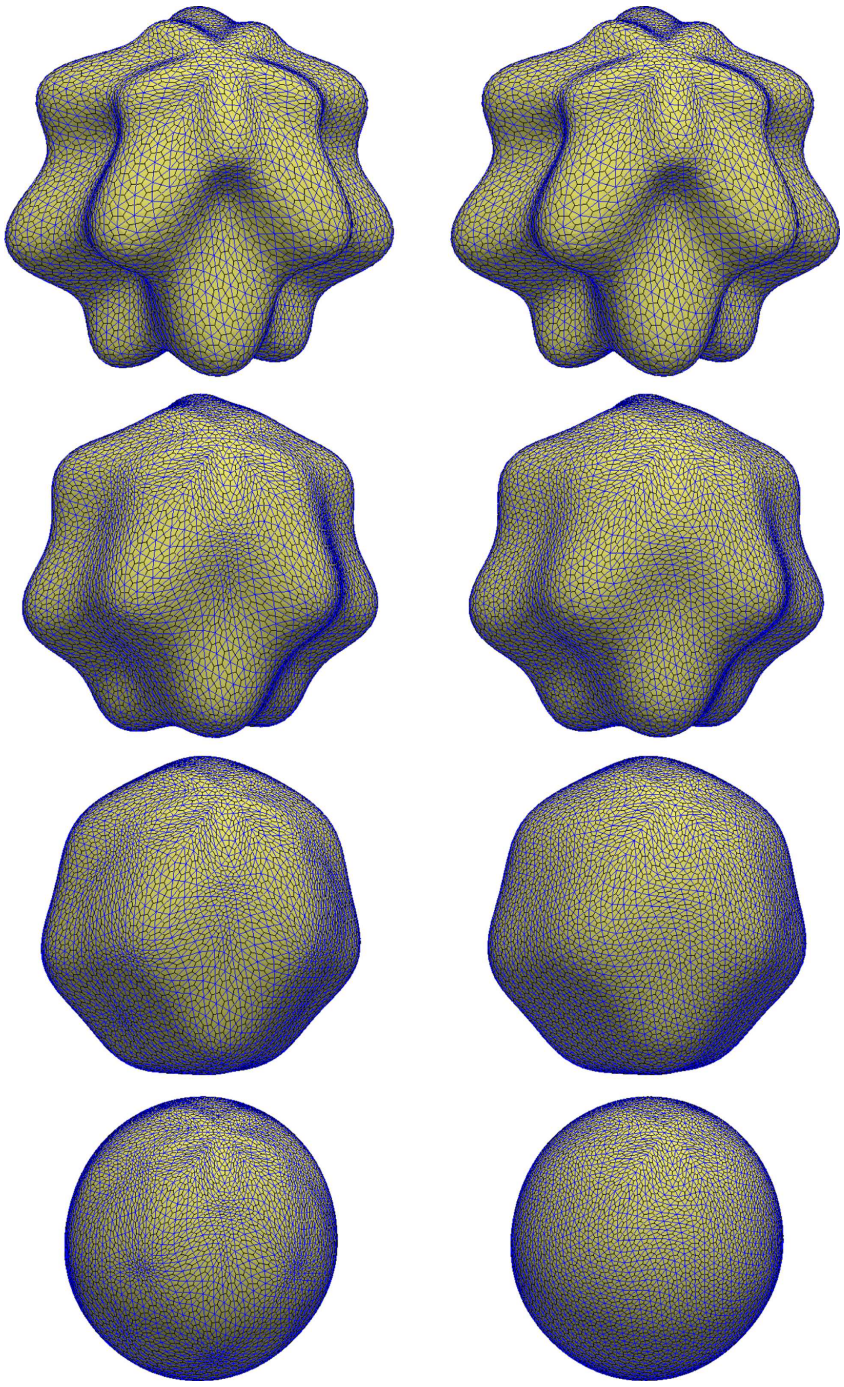

FIGURE 23. The mean curvature flow of a bumpy sphere. *Left column*: the case with no tangential redistribution. *Right column*: the evolution with asymptotically uniform tangential redistribution with $\omega = 100$. The selected time steps are $n = 0, 20, 50, 128$.

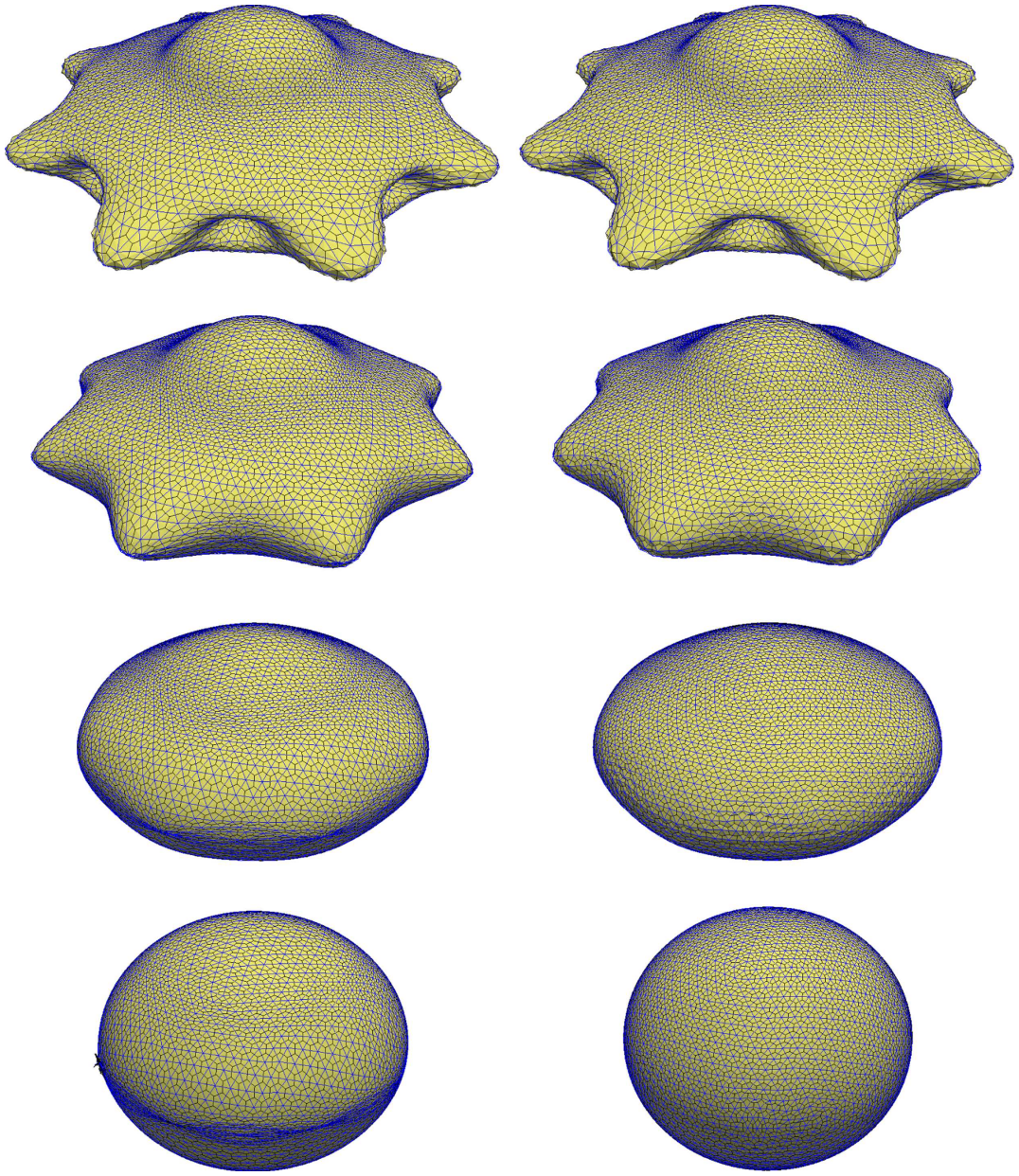

FIGURE 24. The volume preserving mean curvature flow of a cymling-like shape with $n_V = 7682$, $n_F = 2562$ and $n_T = 5120$. Both F- and T-finite volume meshes are displayed. *Left column*: the case with no tangential redistribution. *Right column*: the evolution with asymptotically uniform tangential redistribution with $\omega = 100$. The selected time steps are $n = 0, 10, 50, 300$.

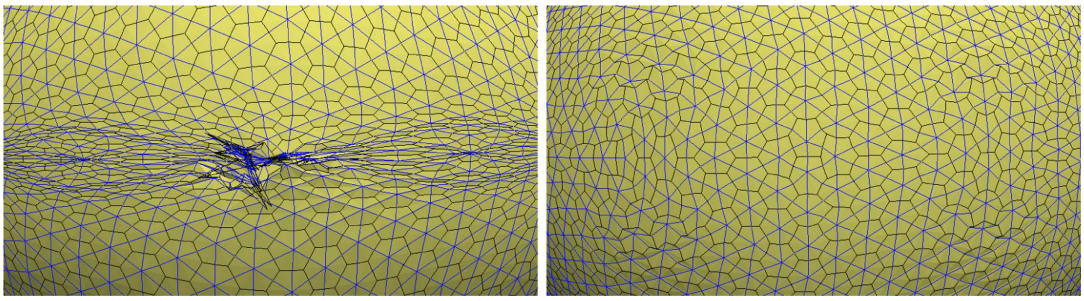

FIGURE 25. Detail of the mesh of the evolved cymling-like shape in time step $n = 300$. *Left panel*: the case with no tangential redistribution. *Right panel*: the case with asymptotically uniform tangential redistribution.

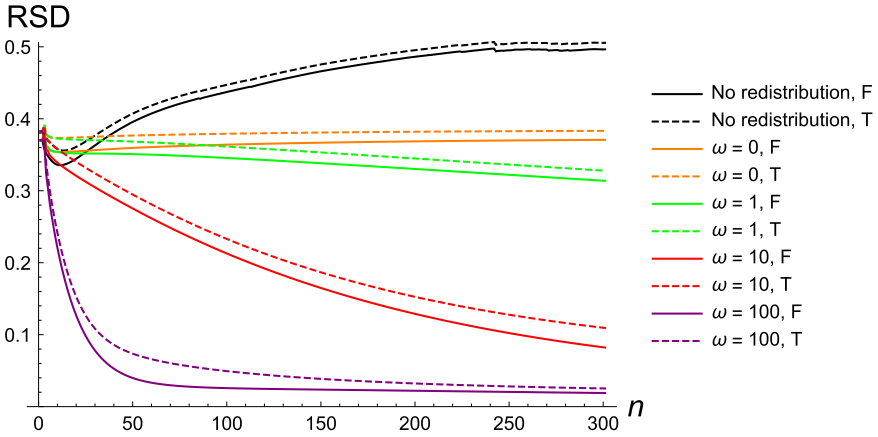

FIGURE 26. The evolution of relative standard deviation (RSD) of the covolume areas for the evolution of cymling-like shape. The solid lines correspond to $\mathrm{RSD}^{F,n}$ and dashed lines correspond to $\mathrm{RSD}^{T,n}$.

5.2. Surfaces with boundary

In this section we use the mean curvature flow to construct approximations of several minimal surfaces with given set of boundary curves. The first experiment is a cylinder evolving to a catenoid. The distance between unit boundary circles is set to 1.11. We use a discretization with $n_V = 600$, $n_F = 216$ and $n_T = 384$, see Figure 27.

The evolution with $t_f = 0.5$ and $\tau = 0.0025$ and no tangential redistribution is shown in Figure 28. The results seem satisfying, however, at much later time steps we can observe an unwanted tangential motion of T-vertices and a degeneration of the diamond mesh (Fig. 29). To describe this behaviour quantitatively we compute the average tangential and normal speeds of vertices throughout the evolution. The normal speed of a F-vertex can be calculated as

$$\|v_{N,i}^F\| = v_i^F \cdot N_i^F, \qquad \text{with} \qquad v_i^F = \frac{F_i^n - F_i^{n-1}}{\tau}, \tag{5.9}$$

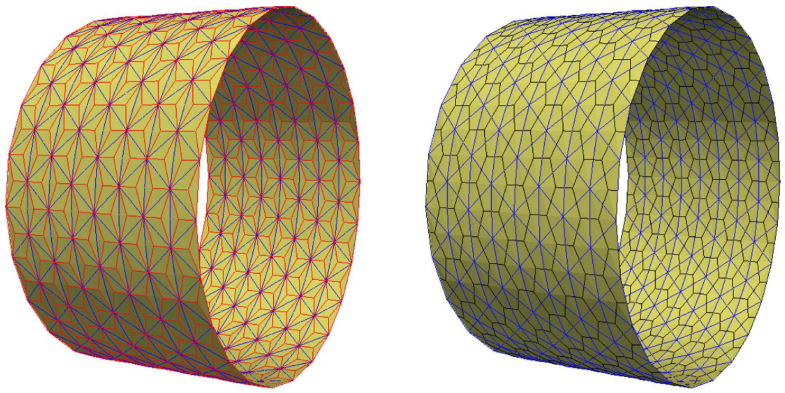

FIGURE 27. The discretized cylinder with $n_V = 600$, $n_F = 216$ and $n_T = 384$. *Left panel*: diamond mesh and finite volume mesh for T-vertices. *Right panel*: finite volume meshes for both F- and T-vertices.

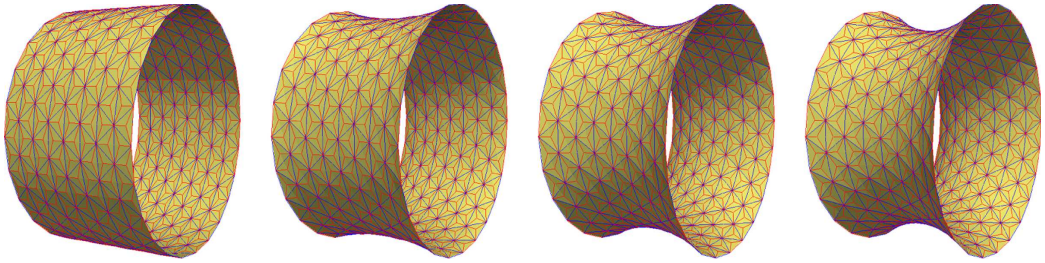

FIGURE 28. The evolution of a cylinder to catenoid. The selected time steps are $n = 0, 40, 100, 200$.

where N_i^F is an approximate normal to the surface at the vertex F_i computed by (4.10). The tangential speed of a F-vertex can be calculated as

$$\|v_{T,i}^F\| = \|v_i^F - (v_i^F \cdot N_i^F)N_i^F\|. \tag{5.10}$$

The computation for T-vertices is analogous. The average tangential and normal speeds of both F- and T-vertices are plotted in Figure 30. We can see that there are nonzero average tangential speeds $\langle v_T^F \rangle$, $\langle v_T^T \rangle$ which are initially about 2–3 orders of magnitude lower than the average normal speeds $\langle v_N^F \rangle$, $\langle v_N^T \rangle$. The normal speeds initially tend to zero as expected (the catenoid is a minimal surface and minimal surfaces are stationary solutions of the mean curvature flow. Therefore when time tends to infinity, the velocity should vanish). In contrast, the average tangential speeds do not, which results in the degeneration of the diamond cells (Fig. 29). As the evolution proceeds and the normal speeds decrease, the nondecreasing $\langle v_T^T \rangle$ becomes dominant and eventually causes the crash of the computation process.

A numerical tangential velocity is not uncommon and it is also present in the cotangent scheme. Due to distretization errors, the discretized normal velocity vector $v_N = \triangle_\varphi \varphi$ does not necessarily point in the normal direction and a numerical tangential velocity appears, see Section 2.4. We eliminate the numerical tangential motion in the following section.

Elimination of the numerical tangential velocity. In Section 2.4 we prepared a tool for elimination of the numerical tangential velocity. We discretize the model (2.33) in time domain adopting the semi-implicit approach which gives

$$\varphi^n - \triangle_{\varphi^{n-1}} \varphi^n = \varphi^{n-1} - \tau\big(h^{n-1} - (h^{n-1} \cdot N^{n-1})N^{n-1}\big).$$

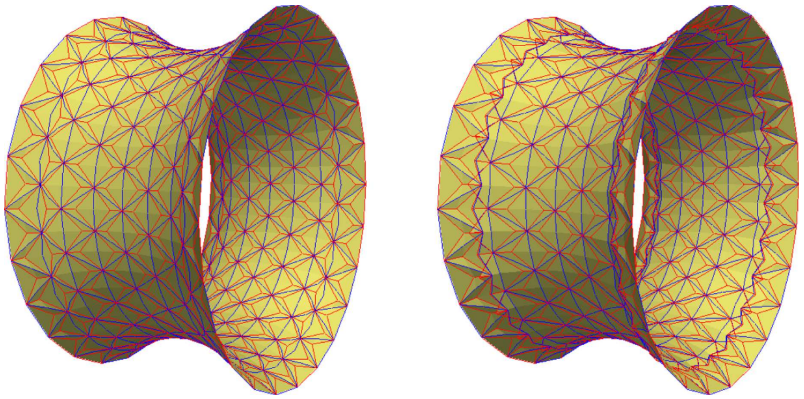

FIGURE 29. A degeneration of the diamond mesh. The selected time steps are $n = 580, 640$.

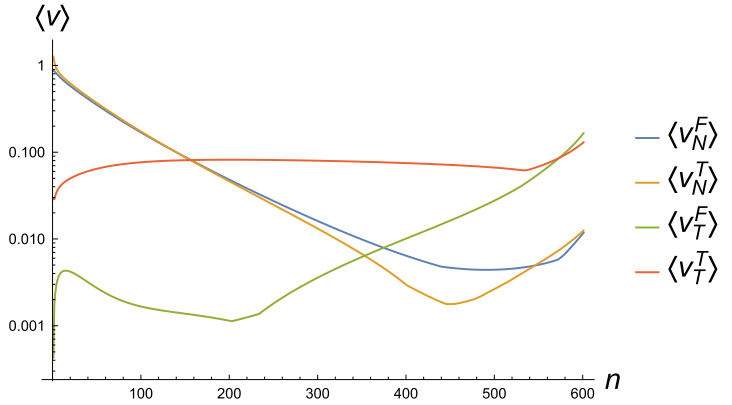

FIGURE 30. The average speed of vertices during the evolution of a cylinder using the DDFV method. In the figure $\langle v_N^F \rangle$, $\langle v_N^T \rangle$ denote the average normal and $\langle v_T^F \rangle$, $\langle v_T^T \rangle$ the average tangential speeds of F- and T-vertices respectively.

After the space discretization analogous to Section 4.1 we obtain the equation for F-vertices

$$\mathfrak{a}_i^{F,n-1} F_i^n + \sum_{p=1}^{m_i} \mathfrak{b}_{i,p}^{F,n-1} F_{i,p}^n + \sum_{p=1}^{m_i} \mathfrak{c}_{i,p}^{F,n-1} T_{i,p}^n = F_i^{n-1} - \tau \left(h_i^{F,n-1} - \left(h_i^{F,n-1} \cdot N_i^{F,n-1} \right) N_i^{F,n-1} \right) \tag{5.11}$$

for $i = 1, \dots, n_F$, where $h_i^{F,n-1}$ is computed by formula (4.27) and coefficients $\mathfrak{a}_i^{F,n-1}$, $\mathfrak{b}_{i,p}^{F,n-1}$, $\mathfrak{c}_{i,p}^{F,n-1}$ are defined in (4.33). For T-vertices we have a formula analogous to (5.11). Note that the system differs from the system (4.32), (4.36) in the right-hand side only.

Experiments with eliminated numerical tangential velocity. In all experiments in the rest of the section we eliminated the numerical tangential velocity using the technique presented above.

Figure 31 shows the experiment with cylinder evolving to the catenoid (with no tangential redistribution). We do not observe any degeneration of the mesh.

The average tangential and normal speeds of both F and T-vertices are plotted in Figure 32. We can see that there is still some nonzero tangential velocity $\langle v_T^F \rangle$, $\langle v_T^T \rangle$ (caused by the semi-implicit time discretization) but, what is crucial, it gradually vanishes during the evolution.

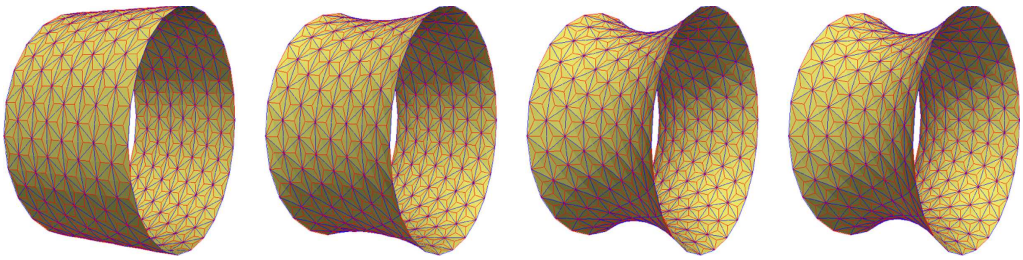

FIGURE 31. The evolution of a cylinder. The selected time steps are $n = 0, 40, 200, 640$.

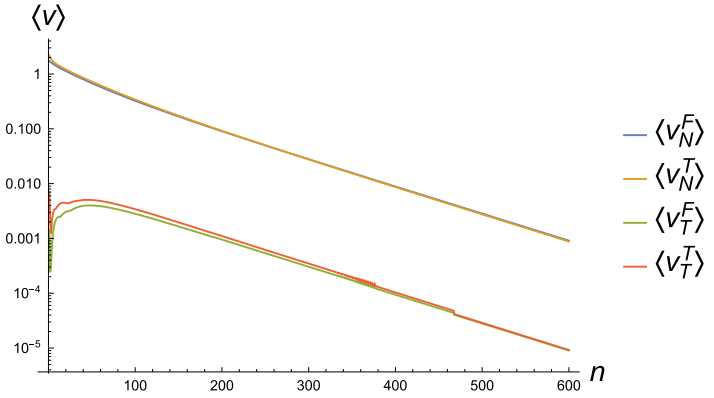

FIGURE 32. The average speed of vertices during the evolution of the cylinder using the DDFV method with eliminated tangential velocity.

The second experiment is a hemisphere with radius equal to 1 and with $n_V = 401$, $n_F = 145$, $n_T = 256$ evolving into the unit disk. The final time and time step were set to $t_f = 1.5$ and $\tau = 0.0025$ respectively. We performed experiments with both no tangential redistribution and with asymptotically uniform tangential redistribution with $\omega = 10$. The evolution is plotted in Figure 33 with top view of the final state in Figure 34.

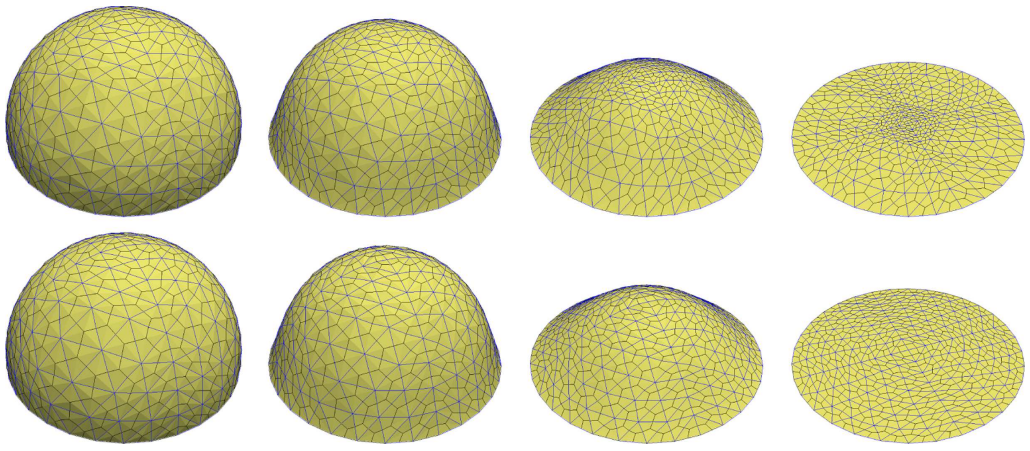

FIGURE 33. The evolution of a hemisphere. *First row*: the evolution with no tangential redistribution. *Second row*: the evolution with asymptotically uniform tangential redistribution with $\omega = 10$. The selected time steps are $n = 0, 20, 80, 600$.

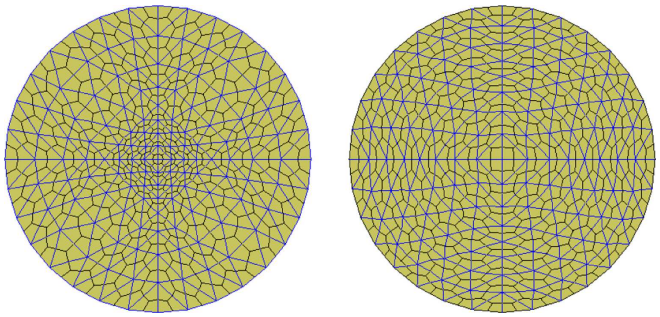

FIGURE 34. Comparison of the meshes in final time step $n = 600$. *Left panel*: no redistribution. *Right panel*: asymptotically uniform redistribution with $\omega = 10$.

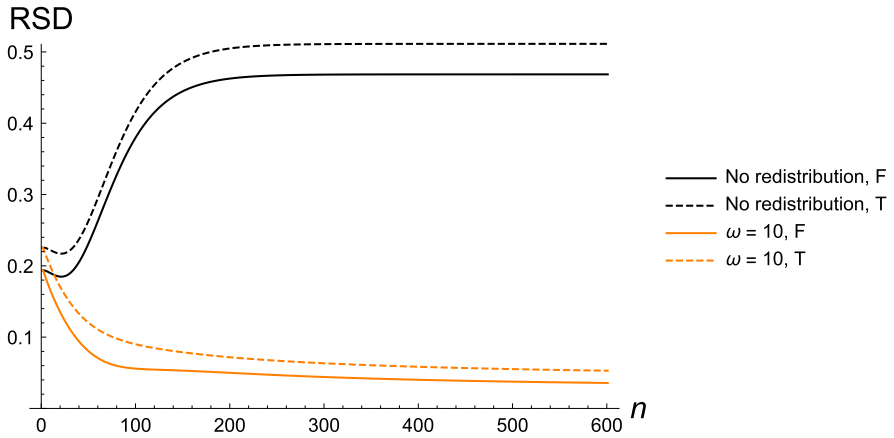

FIGURE 35. The evolution of relative standard deviation of the covolume areas during the evolution of the hemisphere. The solid lines correspond to $\mathrm{RSD}^{F,n}$ and dashed lines to $\mathrm{RSD}^{T,n}$.

In the case with no redistribution we observe a typical contraction of the mesh cells in the middle of the surface. The evolution of the relative standard deviation (RSD) of the covolume areas is plotted in Figure 35.

The third experiment is the evolution of a surface with a sinusoidal boundary curve Γ parametrized as

$$\Gamma(u) = \big(\cos u, \sin u, 0.2 \sin 6u\big),$$

where $u \in [0, 2\pi]$. The initial condition X^0 is parametrized as

$$\begin{aligned} x(r,\phi) &= r\cos\phi, \\ y(r,\phi) &= r\sin\phi, \\ z(r,\phi) &= 0.2\big(r^8(\sin 6\phi + 1) - 1\big), \end{aligned}$$

where $\phi \in [0, 2\pi]$ and $r \in [0, 1]$. We use a discretization with $n_V = 2353$, $n_F = 817$ and $n_T = 1536$ (see Fig. 36). We set to $t_f = 1.0$ and $\tau = 0.0025$. We performed experiments with both no redistribution and with asymptotically uniform redistribution with $\omega = 100$. The final minimal surface ($n = 400$) is shown in Figure 37. The difference in uniformity of the mesh is evident particularly in the regions near the top waves of the boundary curve Γ. The mesh cells near the boundary are more elongated in case with no redistribution.

In the last example we construct a minimal surface with topology of the Costa's surface (see [8]). The initial condition with $n_V = 4124$, $n_F = 1438$ and $n_T = 2686$ is plotted in Figure 38.

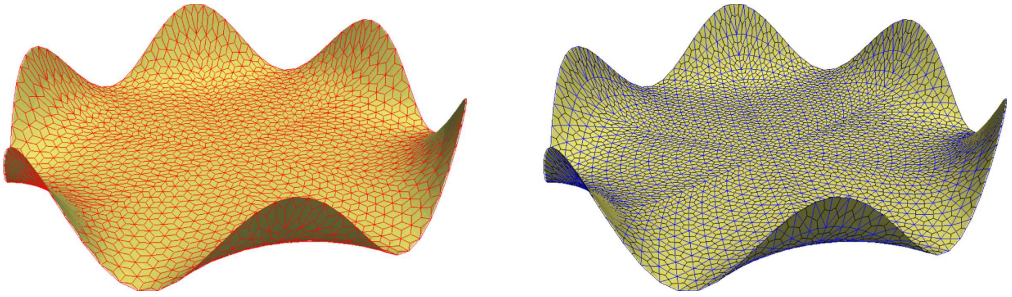

FIGURE 36. The initial condition of a surface with sinusoidal boundary. *Left panel*: the diamond mesh, *right panel*: edges of finite volumes for F- and T-vertices.

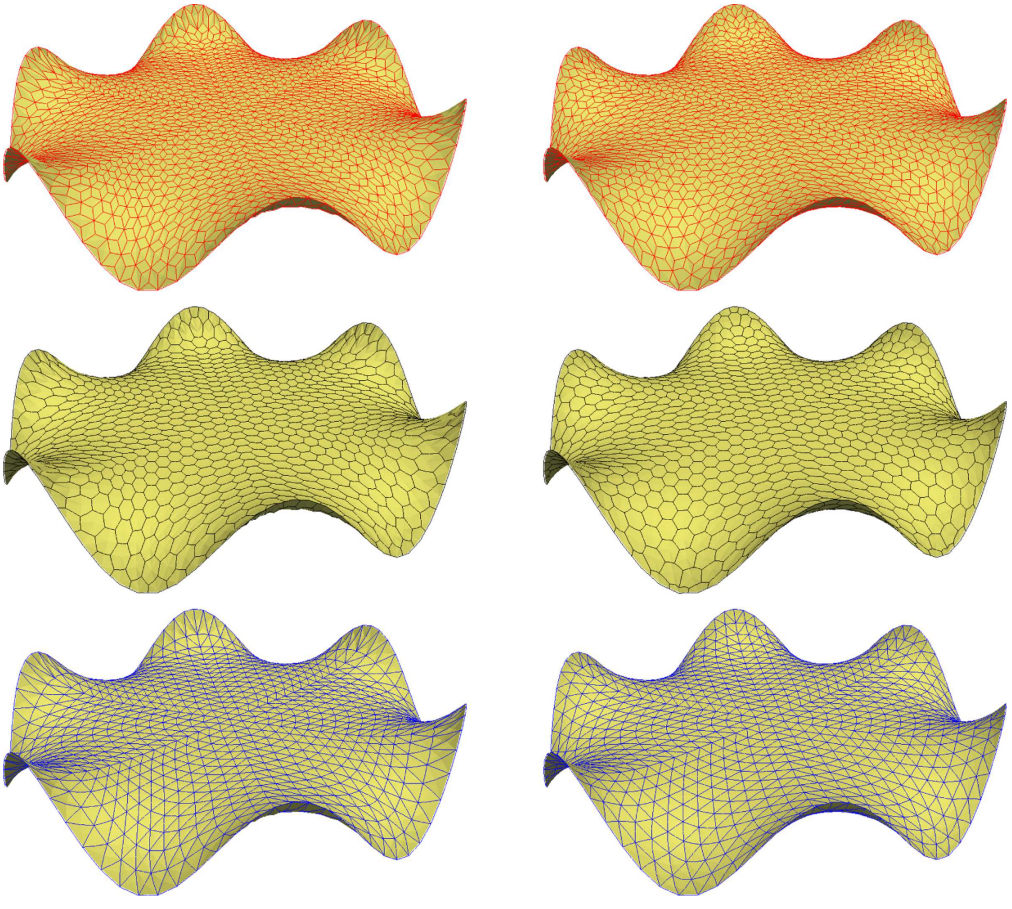

FIGURE 37. The evolved surface with sinusoidal boundary in time step $n = 400$. *Left column*: the case with no tangential redistribution. *Right column*: the case with asymptotically uniform redsitribution with $\omega = 100$. *First row*: the diamond mesh, *second row*: the mesh of F-covolumes and *third row*: depicts the mesh of T-covolumes.

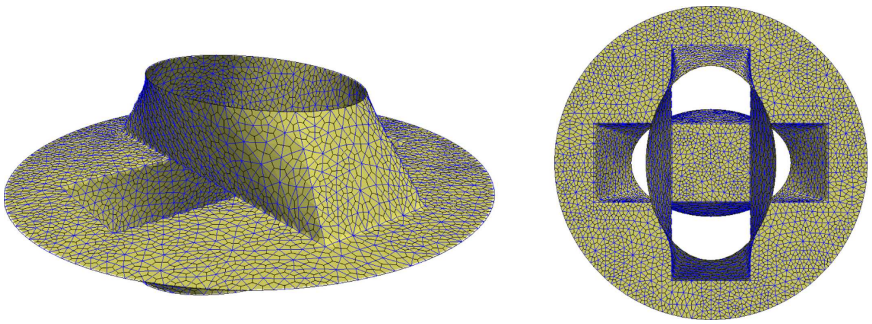

FIGURE 38. Initial condition for construction of the "Costa's surface".

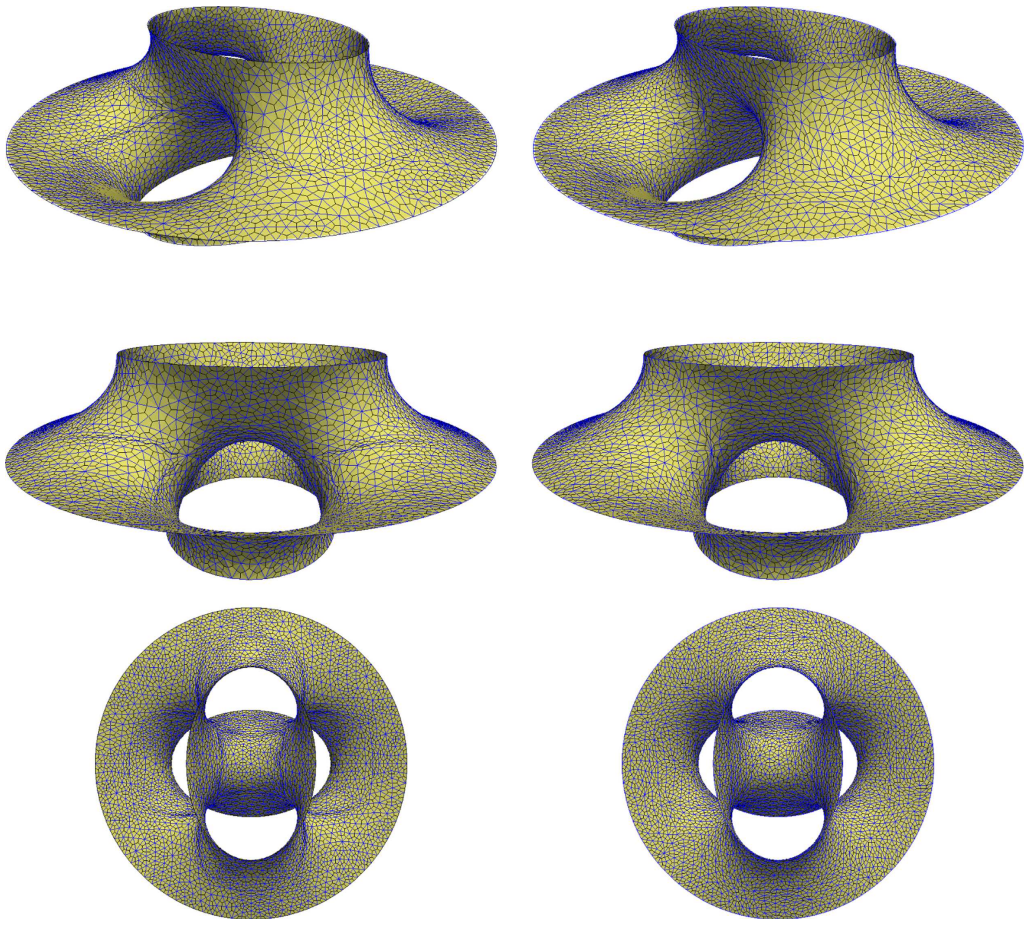

FIGURE 39. Constructed "Costa's surface" from several viewing angles. *Left column*: the case with no tangential redistribution. *Right column*: the case with asymptotically uniform redsitribution with $\omega = 5$.

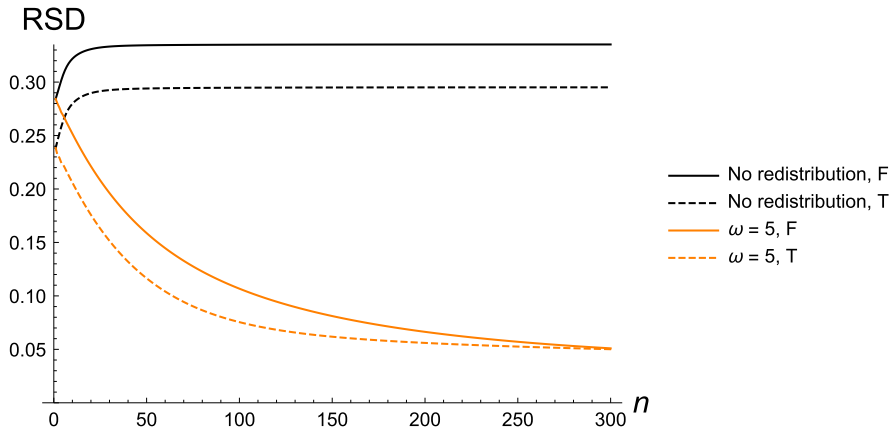

FIGURE 40. The evolution of relative standard deviation (RSD) of the covolume areas during construction of "Costa's surface". The solid lines correspond to $\mathrm{RSD}^{F,n}$ and the dashed lines correspond to $\mathrm{RSD}^{T,n}$.

The boundary $\Gamma = \partial X^0$ consists of three curves $\Gamma = \Gamma_1 \cup \Gamma_2 \cup \Gamma_3$, where

$$\begin{aligned} \Gamma_1(u) &= (4\cos u, 4\sin u, 0), \\ \Gamma_2(u) &= (2.25\cos u, 1.5\sin u, -1.5), \\ \Gamma_3(u) &= (1.5\cos u, 2.25\sin u, 1.5), \end{aligned} \tag{5.12}$$

with $u \in (0, 2\pi)$ for all curves. The parameters were set to $t_f = 1.5$, $\tau = 0.01$ and $\omega = 5$. In Figure 39 we see the final approximation of the minimal surface. In case with no redistribution we observe worse quality of the mesh in regions of higher initial curvature (ridges of the initial surface). The evolution of RSD is plotted in Figure 40.

6. Conclusions

In this paper we derived a Discrete duality finite volume (DDFV) method for solving the mean curvature flow of surfaces in $\mathbb{R}^3$. Our method removes the non-uniqueness of the finite volumes described in section the introduction. We added a suitable tangential velocity to the model in order to redistribute the mesh points along the surface in order to improve the quality of the mesh. We applied the mean curvature flow equipped with the area-oriented tangential redistribution to the problem of finding a minimal surface with given set of boundary curves. Approximations of several minimal surfaces were computed.

There are many issues left for a further research. It could be useful to extend the model by suitable advection term and use the DDFV method in applications (*e.g.* image processing). A tangential redistribution controlling also the shape of mesh cells (not only the areas) and incorporation of mesh topology changing operations (to eliminate high-valency vertices) could also improve the performance of the method in some cases. In a further perspective, it would be interesting, not to impose the choice of triangulations as the basic tool of representing discrete surfaces within the DDFV approach, but extend the method to general polygonal meshes.

Acknowledgements. This work was supported by the projects APVV-15-0522 and VEGA 1/0709/19.

References

[1] L. Alvarez, F. Guichard, P.L. Lions and J.M. Morel, Axioms and fundamental equations of image processing. *Arch. Ration. Mech. Anal.* **123** (1993) 199–257.

[2] J. Barrett, H. Garcke and R. Nürnberg, On the parametric finite element approximation of evolving hypersurfaces in r3. *J. Comput. Phys.* **227** (2008) 4281–4307.

[3] J. Barrett, H. Garcke and R. Nürnberg, The approximation of planar curve evolutions by stable fully implicit finite element schemes that equidistribute. *Numer. Methods Partial Differ. Equ.* **27** (2011) 1–30.

[4] M. Bauer, P. Harms and P.W. Michor, Almost local metrics on shape space of hypersurfaces in n-space. *SIAM J. Imaging Sci.* **5** (2012) 244–310.

[5] H. Benninghoff and H. Garcke, Efficient image segmentation and restoration using parametric curve evolution with junctions and topology changes. *SIAM J. Imaging Sci.* **7** (2014) 1451–1483.

[6] H. Benninghoff and H. Garcke, Segmentation and restoration of images on surfaces by parametric active contours with topology changes. *J. Math. Imaging Vision* **55** (2016) 105–124.

[7] V. Caselles, R. Kimmel and G. Sapiro, Geodesic active contours. *Int. J. Comput. Vision* **22** (1997) 61–79.

[8] A. Costa, Examples of a complete minimal immersion in r^3 of genus one and three embedded ends. *Bil. Soc. Bras. Mat.* **15** (1984) 47–54.

[9] Y. Coudière, J.-P. Vila and P. Villedieu, Convergence rate of a finite volume scheme for a two dimensional convection-diffusion problem. *ESAIM: M2AN* **33** (1999) 493–516.

[10] S. Delcourte, K. Domelevo and P. Omnes, A discrete duality finite volume approach to hodge decomposition and div–curl problems on almost arbitrary two–dimensional meshes. *SIAM J. Numer. Anal.* **45** (2007) 1142–1174.

[11] K. Domelevo and P. Omnes, A finite volume method for the laplace equation on almost arbitrary two-dimensional grids. *ESAIM: M2AN* **39** (2005) 1203–1249.

[12] G. Dziuk, An algorithm for evolutionary surfaces. *Numer. Math.* **58** (1990) 603–611.

[13] G. Dziuk and J.E. Hutchinson, The discrete plateau problem: convergence results. *Math. Comput.* **68** (1999) 519–546.

[14] G. Dziuk and C.M. Elliott, Finite elements on evolving surfaces. *IMA J. Numer. Anal.* **27** (2007) 262–292.

[15] C.M. Elliott and H. Fritz, On algorithms with good mesh properties for problems with moving boundaries based on the harmonic map heat flow and the deturck trick. *SMAI J. Comput. Math.* **2** (2016) 141–176.

[16] L.C. Evans and J. Spruck, Motion of level sets by mean curvature. *J. Differ. Geom.* **33** (1991) 635–681.

[17] R. Eymard, T. Gallouët and R. Herbin, Finite volume methods. In: Solution of Equation in $\mathbb{R}^n$ (Part 3), Techniques of Scientific Computing (Part 3). Vol. 7 of Handbook of Numerical Analysis. Elsevier (2000) 713–1018.

[18] F. Hermeline, A finite volume method for the approximation of diffusion operators on distorted meshes. *J. Comput. Phys.* **160** (2000) 481–499.

[19] T.Y. Hou, I. Klapper and H. Si, Removing the stiffness of curvature in computing 3-D filaments. *J. Comput. Phys.* **143** (1998) 628–664.

[20] T.Y. Hou, J.S. Lowengrub and M.J. Shelley, Removing the stiffness from interfacial flows with surface tension. *J. Comput. Phys.* **114** (1994) 312–338.

[21] M. Húska, M. Medľa, K. Mikula, P. Novysedlák and M. Remešíková, A new form-finding method based on mean curvature flow of surfaces. *Proc. Conf. Algoritmy* (2015) 120–131.

[22] X. Jiao, A. Colombi, X. Ni and J. Hart, Anisotropic mesh adaptation for evolving triangulated surfaces. *Eng. Comput.* **26** (2010) 363–376.

[23] M. Kimura, Numerical analysis of moving boundary problems using the boundary tracking method. *Jpn J. Ind. Appl. Math.* **14** (1997) 373–398.

[24] C. Mantegazza, Lecture Notes on Mean Curvature Flow. Springer Basel, Basel (2011).

[25] M. Meyer, M. Desbrun, P. Schröder and A.H. Barr, Discrete differential-geometry operators for triangulated 2-manifolds. In: Visualization and Mathematics III. Edited by H.-C. Hege and K. Polthier. Springer Berlin Heidelberg, Berlin, Heidelberg (2003) 35–57.

[26] K. Mikula, N. Peyriéeras, M. Remešíková and M. Smíšek, 4D numerical schemes for cell image segmentation and tracking, edited by J. Fořt, J. Fürst, J. Halama, R. Herbin, and F. Hubert. In: Finite Volumes for Complex Applications VI Problems & Perspectives. Springer Berlin Heidelberg, Berlin, Heidelberg (2011) 693–701.

[27] K. Mikula, M. Remešíková, P. Sarkoci and D. Ševčovič, Manifold evolution with tangential redistribution of points. *SIAM J. Sci. Comput.* **36** (2014) A1384–A1414.

[28] K. Mikula and J. Urbán, 3D curve evolution algorithm with tangential redistribution for a fully automatic finding of an ideal camera path in virtual colonoscopy. In: Scale Space and Variational Methods in Computer Vision. Edited by A.M. Bruckstein, B.M. ter Haar Romeny, A.M. Bronstein, and M.M. Bronstein. Springer Berlin Heidelberg, Berlin, Heidelberg (2012) 640–652.

[29] K. Mikula and D. Ševčovič, A direct method for solving an anisotropic mean curvature flow of plane curves with an external force. *Math. Methods Appl. Sci.* **27** (2004) 1545–1565.

[30] K. Mikula and D. Ševčovič, Evolution of curves on a surface driven by the geodesic curvature and external force. *Appl. Anal.* **85** (2006) 345–362.

[31] S. Morigi, Geometric surface evolution with tangential contribution. Special Issue Dedicated to William B. Gragg on the Occasion of His 70th Birthday. *J. Comput. Appl. Math.* **233** (2010) 1277–1287.

[32] P. Mullen, P. Memari, F. Goes and M. Desbrun, Hot: hodgeoptimized triangulations. *ACM Trans. Graph.* **30** (2011) 103.
[33] W.W. Mullins, Two-dimensional motion of idealized grain boundaries. *J. Appl. Phys.* **27** (1956) 900–904.
[34] A. Nealen, T. Igarashi, O. Sorkine and M. Alexa, Laplacian mesh optimization (2006) 381–389.
[35] S. Osher and R.P. Fedkiw, The Level Set Methods and Dynamic Implicit Surfaces. Springer-Verlag, Berlin, **57** (2004).
[36] J. Pełczyński and P. Wawruch, Facade shaping inspired by scherk's minimal surfaces. *XXIV R-S-P seminar, Theoretical Foundation of Civil Engineering (24RSP) (TFoCE 2015). Proc. Eng.* **111** (2015) 632–636.
[37] U. Pinkall and K. Polthier, Computing discrete minimal surfaces and their conjugates. *Exp. Math.* **2** (1993) 15–36.
[38] J.A.F. Plateau, Statique expérimentale et téoretique des liquides soumis aux seule forces moléculaires. Gauthier-Villars, Paris (1873).
[39] H. Schumacher and M. Wardetzky, Variational convergence of discrete minimal surfaces. *Numer. Math.* (2016).
[40] J.A. Sethian, Level Set Methods and Fast Marching Methods: Evolving Interfaces in Computational Geometry, Fluid Mechanics, Computer Vision, and Materials Science. Cambridge University Press, Cambridge (1999).
[41] D. Ševčovič and S. Yazaki, Evolution of plane curves with a curvature adjusted tangential velocity. *Jpn J. Ind. Appl. Math.* **28** (2011) 413.
[42] L. Tomek, K. Mikula and M. Remešíková, Discrete duality finite volume method for mean curvature flow of surfaces. *Proc. of the Conference Algoritmy* (2016) 33–43.
[43] L. Tomek, M. Remešíková and K. Mikula, Computing minimal surfaces by mean curvature flow with area-oriented tangential redistribution. *Acta Math. Univ. Comenianae* **87** (2018) 55–72.
[44] T. Tsuchiya, Discrete solution of the plateau problem and its convergence. *Math. Comput.* **49** (1987) 157–157.
[45] H.A. van der Vorst, Bi-cgstab: a fast and smoothly converging variant of bi-cg for the solution of nonsymmetric linear systems. *SIAM J. Sci. Stat. Comput.* **13** (1992) 631–644.
[46] D. Ševčovič and K. Mikula, Evolution of plane curves driven by a nonlinear function of curvature and anisotropy. *SIAM J. Appl. Math.* **61** (2001) 1473–1501.
[47] T. Wallisser, Other geometries in architecture: bubbles, knots and minimal surfaces. Springer Milan, Milano (2009) 91–111.